crystals

MDPI

Article

Influence of Non-Metallic Inclusions on Local Deformation and Damage Behavior of Modified 16MnCrS5 Steel

Faisal Qayyum [1,*], Muhammad Umar [1,2], Vladislav Elagin [1], Markus Kirschner [1], Frank Hoffmann [1], Sergey Guk [1] and Ulrich Prahl [1]

[1] Institut für Metallformung, Technische Universität Bergakademie Freiberg, 09599 Freiberg, Germany; umar.matrix@gmail.com (M.U.); vladislav.elagin@student.tu-freiberg.de (V.E.); markus.kirschner@imf.tu-freiberg.de (M.K.); frank.hoffmann@imf.tu-freiberg.de (F.H.); sergey.guk@imf.tu-freiberg.de (S.G.); ulrich.prahl@imf.tu-freiberg.de (U.P.)

[2] Department of Mechanical Engineering, Khwaja Fareed University of Engineering and Information Technology, Rahim Yar Khan 64200, Pakistan

* Correspondence: faisal.qayyum@imf.tu-freiberg.de; Tel.: +49-373-139-4073

Abstract: This work investigates a ferrite matrix with multiple non-metallic inclusions to evaluate their influence on the global and local deformation and damage behavior of modified 16MnCrS5 steel. For this purpose, appropriate specimens are prepared and polished. The EBSD technique is used to record local phase and orientation data, then analyze and identify the size and type of inclusions present in the material. The EBSD data are then used to run full phase crystal plasticity simulations using DAMASK-calibrated material model parameters. The qualitative and quantitative analysis of these full phase simulations provides a detailed insight into how the distribution of non-metallic inclusions within the ferrite matrix affects the local stress, strain, and damage behavior. In situ tensile tests are carried out on specially prepared miniature dog-bone-shaped notched specimens in ZEISS Gemini 450 scanning electron microscope with a Kammrath and Weiss tensile test stage. By adopting an optimized scheme, tensile tests are carried out, and local images around one large and several small MnS inclusions are taken at incremental strain values. These images are then processed using VEDDAC, a digital image correlation-based microstrain measurement tool. The damage initiation around several inclusions is recorded during the in situ tensile tests, and damage initiation, propagation, and strain localization are analyzed. The experimental results validate the simulation outcomes, providing deeper insight into the experimentally observed trends.

Keywords: damage mechanics; crystal plasticity; numerical simulation; local deformation behavior; in situ tensile test; VEDDAC; DAMASK; digital image correlation; non-metallic inclusions

Citation: Qayyum, F.; Umar, M.; Elagin, V.; Kirschner, M.; Hoffmann, F.; Guk, S.; Prahl, U. Influence of Non-Metallic Inclusions on Local Deformation and Damage Behavior of Modified 16MnCrS5 Steel. *Crystals* **2022**, *12*, 281. https://doi.org/10.3390/cryst12020281

Academic Editor: Mingyi Zheng

Received: 31 January 2022
Accepted: 15 February 2022
Published: 18 February 2022

1. Introduction

The steel industry is playing an important role in providing about 45% of the raw material to the automotive sector [1]. The advancement in the steel parts used in an automobile is inevitable to competitively improve the strength to weight ratio, fuel economy, and crash safety of cars. Researchers have studied various multi-phase steels to increase the ultimate tensile strength (UTS) and percentage elongation of steels using different thermo-mechanical methods and phase combinations [2,3].

The ever-increasing demand for lightweight materials for the mobility sector has promoted the utilization of the multi-phase phenomenon in steel [4]. For instance, quenched and partitioned (Q&P) steels have shown a UTS up to 1.4 GPa with a uniform elongation of up to 20% [5]. This remarkable combination is desirable during steel formation into sheets and during individual component making with application-based mechanical strength capabilities. Small-sized hard phase inclusions added into the soft ferrite matrix during steel making act as reinforcement participants [6–8]. The common inclusions in the ferrite matrix—i.e., alumina (Al_2O_3), cementite (Fe_3C), manganese sulfide (MnS), and pyrite (Fe_2S)—are very small in size,

in the micron range [9–11]. Alloy steel thus formed with this microstructure, called gear steel, has good machinability and improved hardenability [12,13]. Post-carburizing-quenching case-hardened parts are used in an automobile where a core tensile strength of 800–1100 MPa is needed. Their good wear resistance and low-temperature impact toughness make them usable for piston bolts, camshaft levers, gears, worms, seals, and other sleeve parts [14].

The particle size, distribution, and morphology have a great effect on the overall mechanical properties of these steels [15,16]. MnS with better plasticity and major inclusions in desulphurized alloy steels affects the mechanical anisotropy after being rolled into elongated strips [6]. The deoxidation of the molten steel produces Al_2O_3; being hard, it can act to initiate microcracks and as a propagation source during the application of a load on the component [17]. Moreover, Al_2O_3 can also cause excessive wear of the tool during the machining of the component. Therefore, understanding, controlling, and utilizing the limiting effects of these two inclusions can assist in the material forming processes and producing application-based materials [18–20].

A crystal plasticity-based microstructural approach for investigating material behavior is comparatively more accurate than empirical and phenomenological studies [21–23]. The large-scale crystal plasticity finite element method (CPFEM), with multiple calculation points in a single orientation, can evaluate the average mechanical response of a polycrystalline material. An added advantage of this type of modeling and simulation is the analysis of the local stress and strain behavior to mitigate the concentrations and prolong the global elongation process [24,25].

Although large-scale CPFEM methods are considered important for the true behavior recognition of multi-phase materials, the literature has limited results that can be applied satisfactorily to the mass production of parts [26–31]. Recently, DP steel (martensite in a ferrite matrix) has been studied using the relaxed grain cluster homogenization technique using the Düsseldorf Advanced Material Simulation Kit (DAMASK) [32–34]. The results gave an interesting insight into microstructural evolution during the deformation of heterogeneous multi-phase materials. However, there is still a need for extensive study based on individual phase constituents in the steel matrix to reach a point where industrially required process maps can be generated and utilized for microstructurally informed material production.

This study is a unique combination of various techniques to evaluate the micromechanical response of polycrystalline multi-phase material. Industrially produced modified 16MnCrS5 with alumina, pyrite, and cementite as precipitate phase particles spread all over the ferrite matrix has been used as a starting material. An EBSD map has been generated, and in situ tensile deformation has been performed while recording the local material state at various global stress values. A crystal plasticity-based numerical simulation model built on finite strain theory has been used to study slip-based plastic deformation in a ferrite matrix. The correlation of simulation results with the experimental obtained local material behavior is studied and presented.

The manuscript has been categorized so that Section 1 presents the introduction and background of the study. Section 2 has very brief information about the experimental procedures. The modeling technique with the current numerical simulation procedure with boundary conditions is mentioned in Section 3, while the results are detailed in Section 4. Finally, Section 5 gives a complete discussion of the results compared to the already published literature, while the study's conclusions are presented in Section 6.

2. Methodology

In this work, in situ tensile tests were carried out on specially prepared specimens inside the SEM chamber in a deformation stage. The local EBSD data from the same specimen were used to run a full phase crystal, plasticity-based numerical simulation model. The material's local deformation and damage behavior, especially around an MnS inclusion, was analyzed and compared with the numerical simulation results. This section

contains a complete methodology of the in situ tensile tests, EBSD data collection, and data processing that was carried out.

2.1. In Situ Test Setup and Data Collection

For in situ investigations, a specialized method was adopted based on previously published work by other researchers [35–39]. For in situ testing, tensile specimens according to DIN EN ISO 6892-1 with a length of 50 mm and a thickness of 0.6 mm with notches for strain concentration were prepared as shown in Figure 1c. The samples were cut from the discs using a water jet cutting machine to avoid material wastage and residual stress accumulation on the surfaces during conventional machining. The prepared samples were finely milled to obtain a better edge finish and produce small u-shaped notches in the middle of the neck, as shown in Figure 1c. They were prepared by metallographic polishing. Since the specimens were very thin, a special embedding compound was used during the polishing process that could be dissolved in acetone when heated to 30 °C after the polishing process was complete. As the test specimens' deformed surface was later to be analyzed with digital image correlation software, the test specimens were etched for 5 s in a 3% Nital solution to achieve the required surface contrast. The visual inspection of specimens before testing revealed that only non-deformed inclusions were found on the surface of the specimens, and a few MnS inclusions with an elongated shape were present in the middle of the specimen. Further details about specimen preparation and the achievement of the correct contrast of micrographs using image processing techniques are provided in Appendix A for interested readers.

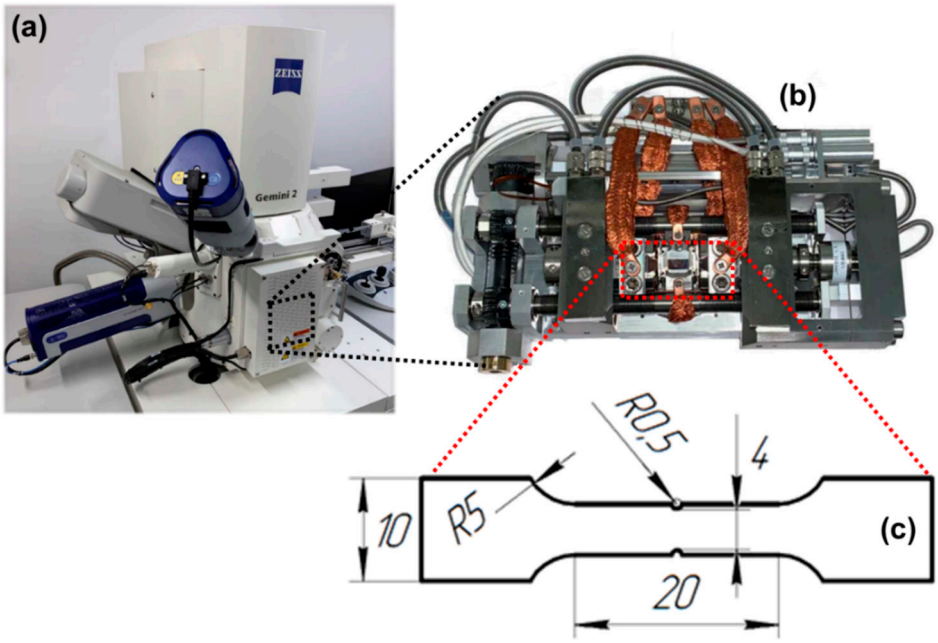

Figure 1. (**a**) ZEISS Gemini SEM 450 scanning electron microscope used (**b**) and the in situ tensile model. (**c**) Geometry of the in situ specimens with notches for the stress concentration, where all the dimensions are in mm.

The overall chemical composition of the current material is shown in Table 1 in comparison with the standard chemical composition of the alloy. It is modified 16MnCrS5 with 50% lower carbon content and 20% more sulfur. Therefore, the strength of this modified material is slightly lower; due to higher sulfur content and less carbon, it contains more MnS inclusions, with some being predominantly large (as discussed later in Sections 2.3 and 2.4).

Table 1. Chemical composition of the investigated modified 16MnCrS5 steel in weight percentage in comparison with standard non-modified 16MnCrS5 steel.

	Element	C	Si	Mn	P	S	Cr	Al	Cu
% Wt.	non-modified	0.16	0.25	1.15	<0.01	0.035	1.00	<0.01	0.03
	modified	0.081	0.038	1.07	<0.01	0.131	1.06	<0.01	0.03

The in situ tensile tests were carried out with a ZEISS Gemini SEM 450 scanning electron microscope using a Kammrath and Weiss tensile test stage, as shown in Figure 1a,b. This module allows in situ data collection during tensile or compressive loading using SE, EBSD, and EDS in the Gemini SEM450 of Carl Zeiss AG. For the experiments, different points on the tensile stress–strain curve were targeted at a forming speed of 8 µm/s, and the specimen was held at various values of stress and strain. At the same time, analyses of the microstructure and chemistry were performed. A series of images was taken during tensile testing. All images were taken with a resolution of 2048 × 1536 pixels. In addition, all photos in the area of interest were taken with a magnification of 11k and WD (working distance) of 16.6 mm with the "InLens" module.

2.2. Selection of Area for Full Phase Simulations

For the crystal structure analysis, the specimens were placed in the Gemini SEM450 from Carl Zeiss AG. The EBSD analysis was performed with an accelerating voltage of 20 kV, a working distance of 11 mm, and a specimen holder pre-tilted by 70°. The magnification was 10,000×. For the EBSD analysis, the Symmetry S2 detector from Oxford Instruments PLC was used. The analysis area was 95.4 µm × 71.8 µm, with a step size of 0.2 µm. The advanced Symmetry S2 EBSD detector utilizes a unique combination of speed (4500 pixels/second), sensitivity (CMOS technology sensor), and diffraction pattern details (1244 × 1024 pixel resolution) to efficiently produce high-quality EBSD data for the selected area, which can then be post-processed to obtain information in the desired format. Modified 16MnCrS5 steel contains inclusions that are quantitatively analyzed and recoded using EDS Ultim MaxX from Oxford Instruments PLC.

The multi-phase steel material Representative Volume Element (RVE) was obtained after EBSD analysis. The data were initially raw and required cleaning for unindexed points due to crystallographic noise at the grain boundaries. This noise was reduced using an intelligent algorithm implemented on the MTEX toolbox with MATLAB [40]. The procedural details of the EBSD data cleaning and the developed algorithm are published elsewhere [41]. Therefore, readers are encouraged to refer to that work for further details.

The ferrite matrix distribution is shown in Figure 2a, and the distributions of alumina (Al_2O_3), cementite (Fe_3C), and manganese sulfide (MnS) concerning the grain boundaries are displayed in Figure 2b. Most of the inclusions detected in this area of the specimens are present on the grain boundaries. This kind of microstructure with appropriately large second phase particles distributed homogeneously on the grain boundaries of adequately large ferrite grains appears to be due to the adopted manufacturing strategy.

2.3. Statistical Analysis of the EBSD Data

A quantitative comparison of the grain shape (aspect ratio) and particle size of the ferrite matrix and inclusions is presented in Figures 3 and 4, respectively. In Figure 3, the aspect ratio of 1 corresponds to almost perfectly round shapes, whereas the higher aspect ratio corresponds to the adequately elongated grain or inclusion. Considering this criterion, the aspect ratio of ferrite grains in Figure 3a predominantly lies between 1–2, except for some grains with a high degree of elongation of >4, which is the normal ferrite microstructure reported in previous literature [42,43]. On the other hand, the inclusions in Figure 3b–d are largely round (aspect ratio = 1), with some particles slightly elongated. There can be two reasons why the manufacturing process yields such inclusion shapes, as reported previously [44], or it can be due to the limitations of the measurement

and magnification chosen in this work. During EBSD analysis, only these slightly large inclusions with round profiles were detected due to the chosen magnification and the set step size. In contrast, very thin and long inclusions were missed.

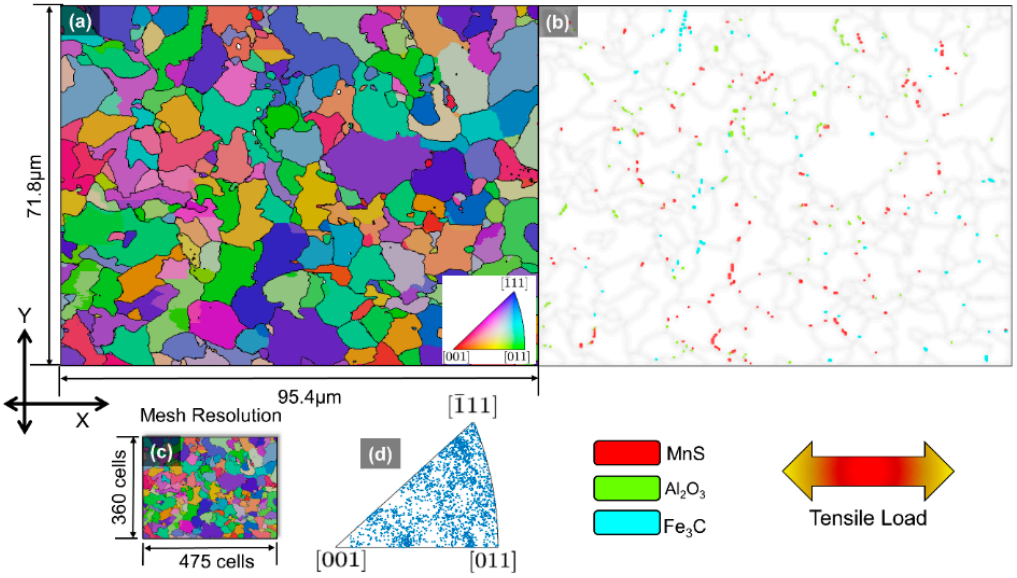

Figure 2. Multi-phase steel specimen. (**a**) IPF for ferrite matrix with BCC crystal structure, with different colors showing different crystallographic orientations. (**b**) Three types of inclusions spread all over the ferrite matrix and (**c**) the mesh resolution showing the grid size for calculation points. (**d**) IPF figure showing orientations of ferrite grain orientations with reference directions.

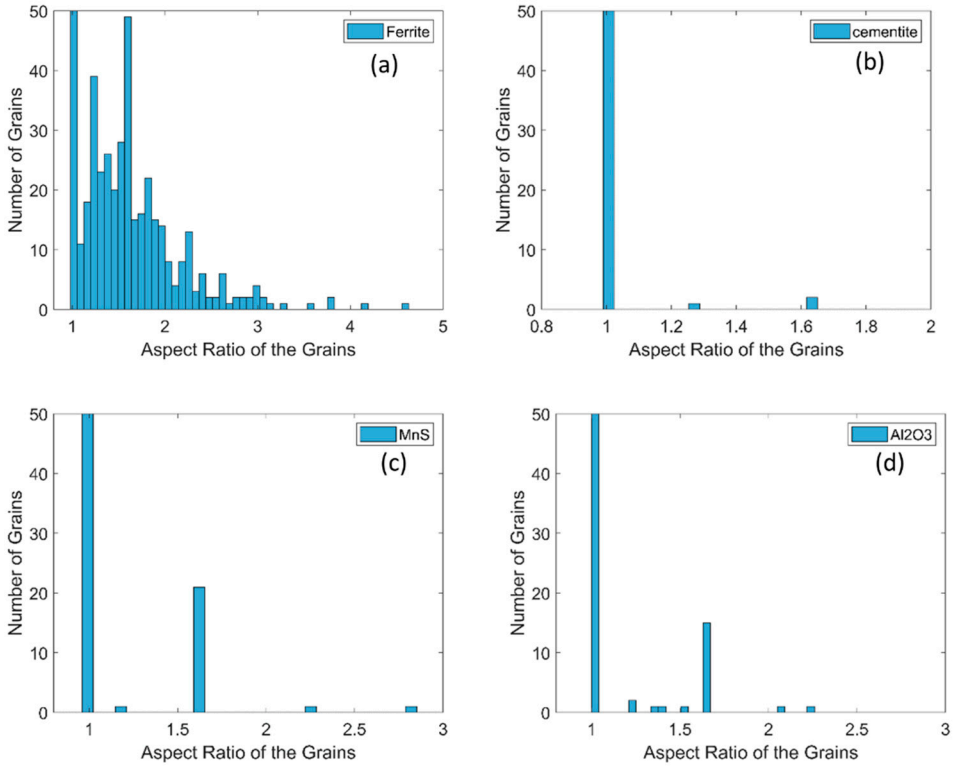

Figure 3. Distribution of aspect ratios of (**a**) ferrite grains, which are relatively larger and have a wider spread; (**b**) cementite inclusions, which are close to 1, with few inclusions at 1.3 and 1.7; (**c**) MnS inclusions are also usually round, with a few with a spread of 2.8; (**d**) Al_2O_3 inclusions are also usually round with an aspect ratio of 1, with some inclusions reaching up to 2.3.

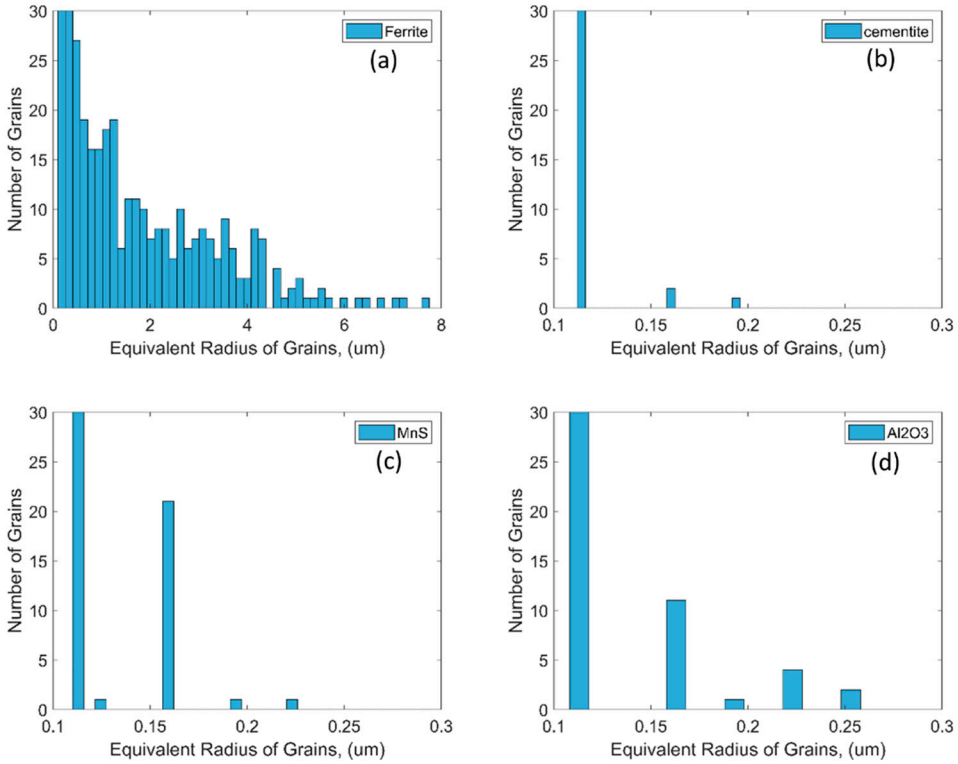

Figure 4. Distribution of grain size in terms of equivalent radius (ER) for (**a**) ferrite, which is biased towards small grains but being widespread reaches up to 8 µm; (**b**) cementite inclusions, which are generally small with sizes close to 0.1 µm, with a few inclusions up to 0.18 µm ER; (**c**) MnS inclusions, which although usually small are in a large number with 0.16 µm ER and a few as large as 0.23 µm. (**d**) The Al_2O_3 inclusions have a large spread with many having sizes close to 0.1 µm and then having a downslope spread up to 0.25 µm ER.

The grain size in Figure 4 is measured in terms of the mean sphere diameter. A significant number of ferrite grains in the selected area for EBSD analysis are below 4 µm, as observed in Figure 4a, and some grains are larger than 6 µm. As shown in Figure 4b–d, the inclusions are comparatively very small. Most inclusions are around 0.1 µm in size, whereas very few are larger than 0.2 µm. Even smaller inclusions may be present within the microstructure but were not detected due to the selected magnification and EBSD measurement step size. This lack of smaller inclusions negligibly alters the material chemistry or local phase distribution and hence is assumed to have almost no effect on the simulation results.

Second phase inclusions have been talked about a great deal in this section. The elemental analysis of an MnS inclusion using EDS analysis is presented in Figure 5 for reference. All the other inclusions—i.e., Al_2O_3 and Fe_3C—have also been identified using the same process.

2.4. Selection of Area, Tools Used, and Methodology Adopted for In Situ Strain Measurement

During the in situ tensile tests, a large, elongated sulfide inclusion (MnS) was analyzed. The inclusion, along with the chemical analysis confirming it to be MnS, is shown in Table 2. The length of the inclusion together with the cavity is about 42.5 µm. The elongated inclusion aligned with the tensile loading axis (horizontal to the shown micrograph) was expected to be prone to severe fracture and was therefore of great interest.

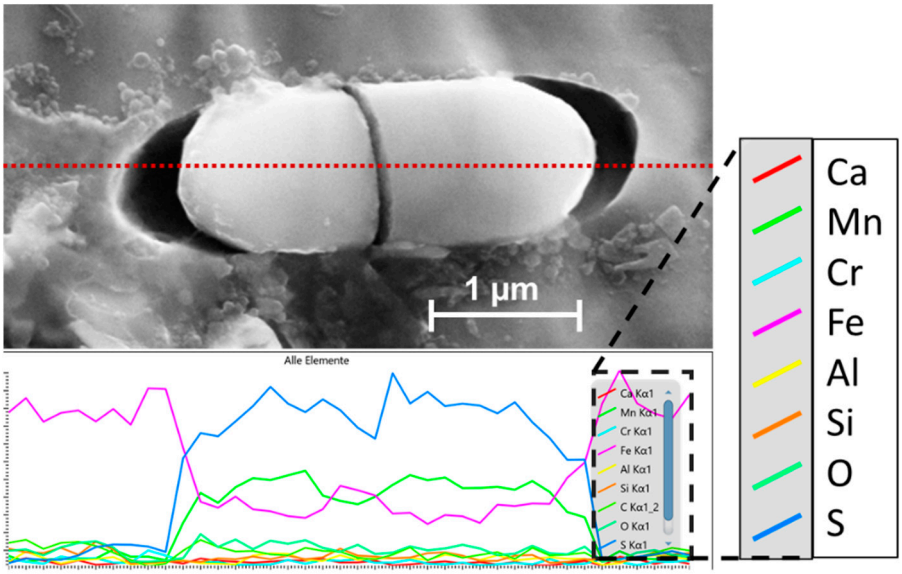

Figure 5. Elemental analysis of the modified 16MnCrS5 steel specimen using EDS to identify the inclusions (the red dotted line represents the line of measurement). The inclusion shows a major concentration of Mn and S; therefore, it is classified as an MnS inclusion.

Table 2. Chemical analysis of inclusion at different points, confirming MnS. The units of the measurement are in mass, %.

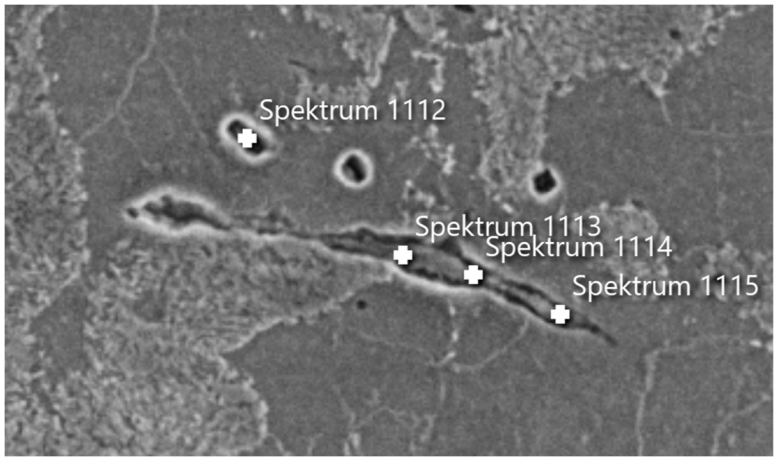

Element	Spectrum 1112	Spectrum 1113	Spectrum 1114	Spectrum 1115
S	10.50	6.46	10.34	14.65
Cr	1.19	1.70	0.95	0.95
Mn	17.06	11.61	17.24	23.48
Fe	69.56	75.98	70.66	60.16
Others	1.69	4.25	0.81	0.76
Total	100.00	100.00	100.00	100.00

The in situ tests come with their own challenge of image acquisition [35–37]. The images taken during the test should have a specific contrast and clear feature identification possibility [45]. To ensure that the images taken during the current tests are of acceptable quality and grayscale distribution, an analysis was performed that has not been included in the main part of the body but is presented in Appendix A. The effect of different settings and attributes is discussed and can be interesting for readers interested in performing such tests themselves. Appendix A also contains detailed information about the local and global strain measurement during experimentation.

The digital image correlation software VEDDAC from Chemnitzer Werkstoffmechanik GmbH was used to process the captured image series. When processing the images, images with strong contrast or sharpness fluctuations were removed from the calculations, and the final set contained images. Two calculation areas were selected during DIC. The first calculation area is shown in Figure 6a, which consists of the matrix around the inclusions and the cavities. The second calculation is the inclusion area and cavities around it, as shown in Figure 6b. The optimal grid sizes for a particular series of images were 9 × 9 pixels (coarse) for the matrix and 5 × 5 pixels for the inclusion (fine). More information about the local strain measurement methodology is provided in Appendix B.

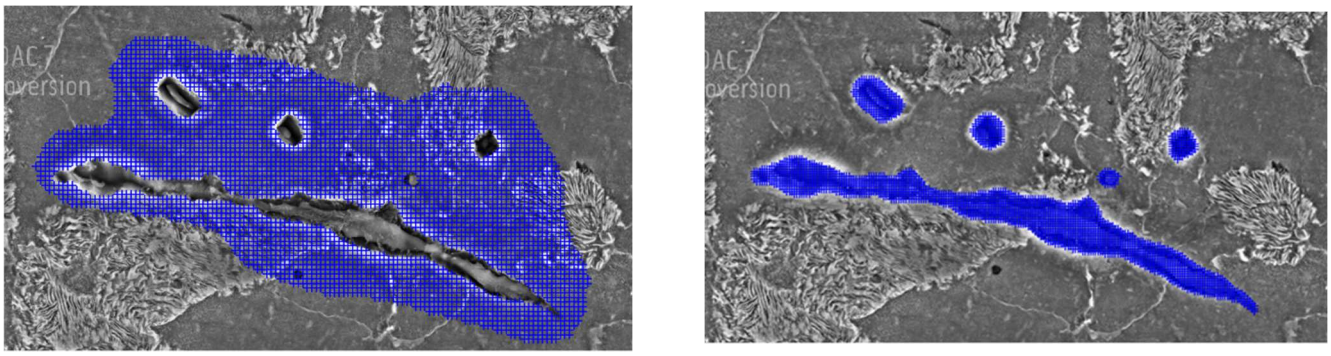

(**a**) (**b**)

Figure 6. Calculation network for digital image correlation (**a**) around non-metallic inclusions (**b**) in non-metallic inclusions and cavity area. In this work, a grid of 9 × 9 pixels (coarse) for the matrix and 5 × 5 pixels for the inclusion (fine) was chosen to get accurate and fully resolved results.

3. Numerical Simulation Model Setup

The EBSD data and the information of each phase's chemical and crystallographic structure were used to model and run a full phase crystal plasticity-based numerical model with calibrated material models. These simulations were used to provide detailed information about the local deformation and damage behavior of this material and how different inclusions, morphologies, and distributions affect the local deformation and damage behaviors. This insight is useful to understand the data from limited in situ tests.

First developed by Hutchinson [46] and later extended by Kalidindi [47], the phenomenological model implemented in the DAMASK framework [33] calculates the plastic deformation by slip planes based on the initial and saturated slip resistance—S_0, S_s, respectively (refer to Table 3). This resistance value for slip systems = 1,2,3 . . . N_{slip} increases from the initial to saturation value depending on the crystal structure specifications and the critical shear value on the slip plane during deformation.

This model uses a mathematical description to correlate the initial deformation gradient (F) with the resulting first Piola–Kirchoff stress tensor (P), as shown in Equations (1) and (2). The elastic part is simplified in the form of the generalized Hook's law, and for the plastic part, it is given with the help of the plastic velocity gradient given in Equation (3).

$$\begin{aligned} \dot{\overline{F}}_{ij} &= \begin{bmatrix} 1 & 0 & 0 \\ 0 & * & 0 \\ 0 & 0 & * \end{bmatrix} \times 10^{-3}\mathrm{s}^{-1} \\ \overline{P}_{ij} &= \begin{bmatrix} * & * & * \\ * & 0 & * \\ * & * & 0 \end{bmatrix} Pa \end{aligned} \tag{1}$$

$$S = CE^e \tag{2}$$

where

S = second Piola–Kirchoff stress tensor;

C = fourth-order elastic stiffness Tensor;
E^e = second-order Langrangian strain tensor.

$$L_p = \sum_{\alpha=1}^{\text{Nslip}} \dot{\gamma}^{\alpha} \left(\mathrm{m}^{\alpha} \otimes \mathrm{n}^{\alpha}\right) \tag{3}$$

The value of the velocity plasticity gradient L_p is dependent on the shear strain γ (Equation (4)), which is a function of the resolved shear stress τ^{α} and slip-resistance on the α slip plane S^{α}.

$$\dot{\gamma}^{\alpha} = \dot{\gamma}_0 \left| \frac{\tau^{\alpha}}{S^{\alpha}} \right|^{n} \operatorname{sgn}(\tau^{\alpha}) \tag{4}$$

and

$\alpha = 1, 2, 3 \cdots, N_{slip}$ (For BCC Ferrite N_{slip} = 24)

A non-conserved damage field φ is governed by the continuous release of the stored mechanical energy density from undamaged to fully damaged conditions in a region; i.e., φ = 1 to φ = 0. In the ductile damage criterion implemented in DAMASK, plastic energy dissipation at a material point is the driving force here for damage flux f_{φ}. Therefore, plastic energy dissipation in the form of the following equation is used:

$$w_{plastic} = \frac{1}{2}\varphi^2 \int M_p.L_p dt. \tag{5}$$

Consequently, the minimization of the total free energy density is responsible for force to drive damage, and it is given as follows:

$$f_{\varphi} = -\left[\frac{\partial w_{plastic}}{\partial \varphi} + \frac{\partial w_{surface}}{\partial \varphi}\right] = \frac{G}{l_c} - \varphi \int M_p.L_p dt. \tag{6}$$

where

G = surface tension of the newly generated damage surface;
l_c = length scale of the diffused surface;
L_p = plastic velocity gradient.

The plastic governing law changes to the following when damage evolution is coupled with dissipated plastic energy:

$$L_p = f\left(\frac{M_p}{\varphi^2}\right) \tag{7}$$

Readers are encouraged to read the pioneering work by the developers of DAMASK for further details and understanding of the model [33,34,48,49]. For instance, a strategy was published recently by Qayyum et al. [50] by choosing an optimal RVE that behaves isotopically yet is small enough to produce fast results for the calibration of the material model parameters of single-phase materials. The strategy comprises a 10 × 10 × 10 size RVE containing 1000 grains, where each point represents a different grain. The RVE adopted from that published methodology is shown in Figure 7a. This RVE was used to calibrate the fitting parameters in the material model by comparing simulation outcomes with the experimental observations, and the results are shown in Figure 7b.

It is observed that the simulation results match well with the experimental observations globally. The dips in the experimental data are positions where the test was stopped and pictorial data were recorded. The adopted and calibrated material model parameters used in this study are shown in Table 3. This set of parameters was used to run full phase simulations and then analyze the local material deformation and damage behavior.

The DAMASK framework is designed to get all the inputs in the form of specifically structured text files with a complete microstructural description of RVE with geometrical details, material behavior attributes, and boundary values. Elastic and plastic phase parameters for ferrite and only elastic parameters of all the inclusions are defined to observe the micromechanical deformation of ferrite caused by stiffness degradation. Ductile damage

criteria have been incorporated in the ferrite matrix as well. The RVE generated by using the EBSD data shown in Figure 2 was subjected to quasi-static tensile load with a strain rate of 10^{-3} s^{-1} in the x-direction.

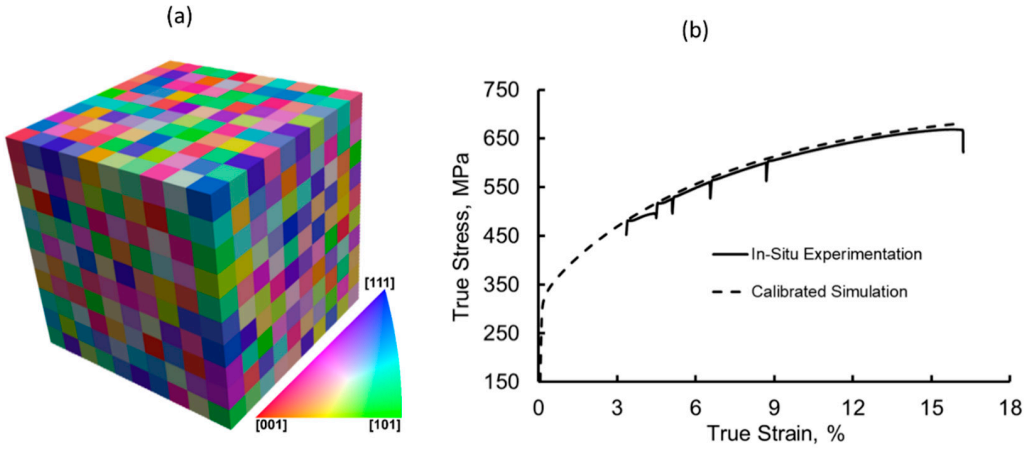

Figure 7. (**a**) 10 × 10 × 10 size RVE containing 1000 individual grain orientations, (**b**) comparison of experimental and simulation flow curves, showing a good match of results.

Table 3. Elastic parameters of second phase inclusions obtained from the literature [10,20,23,26,28,41,51,52] and calibrated parameters of ferrite adopted from the literature [23,26,28,41,52] and adjusted by comparing with the flow curve from in situ tests. The ductile damage parameters were calibrated by comparing them with the in situ test results.

Elastic Parameters of All the Phases		
Parameter	**Value**	**Unit**
Ferrite-$C_{11,}C_{12,}C_{44}$	233.3, 235.5, 128.0	GPa
Fe_3C-$C_{11,}C_{12,}C_{44}$ [17]	375.0, 161.0, 130.0	GPa
MnS-$C_{11,}C_{12,}C_{44}$ [6]	177.3, 117.0, 25.2	GPa
Al_2O_3-$C_{11,}C_{12,}C_{44}$ [10]	496, 109, 206 [18]	GPa
Plastic Parameters of Ferrite Phase		
$\dot{\gamma}_0$	5.6×10^{-4}	ms^{-1}
S_0, [111]	95	MPa
S_s, [111]	222	MPa
S_0, [112]	96	MPa
S_s, [112]	412	MPa
h_o	1	GPa
$h_{\alpha\beta}$	1.0	GPa
n, w	3, 2.0	-
N_{slip}	12, 12	-
N_{twin}	0	-
Ductile Damage Parameters		
Parameter Description	**Value for Ferrite**	**Unit**
Interface energy (g_0)	1.0	Jm^{-2}
Damage mobility coefficient (M)	0.001	s^{-1}
Critical plastic strain (ε_{crit})	0.5	-
Damage rate sensitivity coefficient (P)	10	-
Damage diffusion (D)	1.0	-

4. Results

4.1. Global Results of Numerical Simulation

The global results of the simulation in comparison with experimental observations are shown in Figure 8. The global results are calculated by taking an average of the results at each solution point for each increment. The data are combined in a meaningful way to produce observable trends. The stress and damage evolution with respect to the true global strain in the selected RVE is shown here in Figure 8.

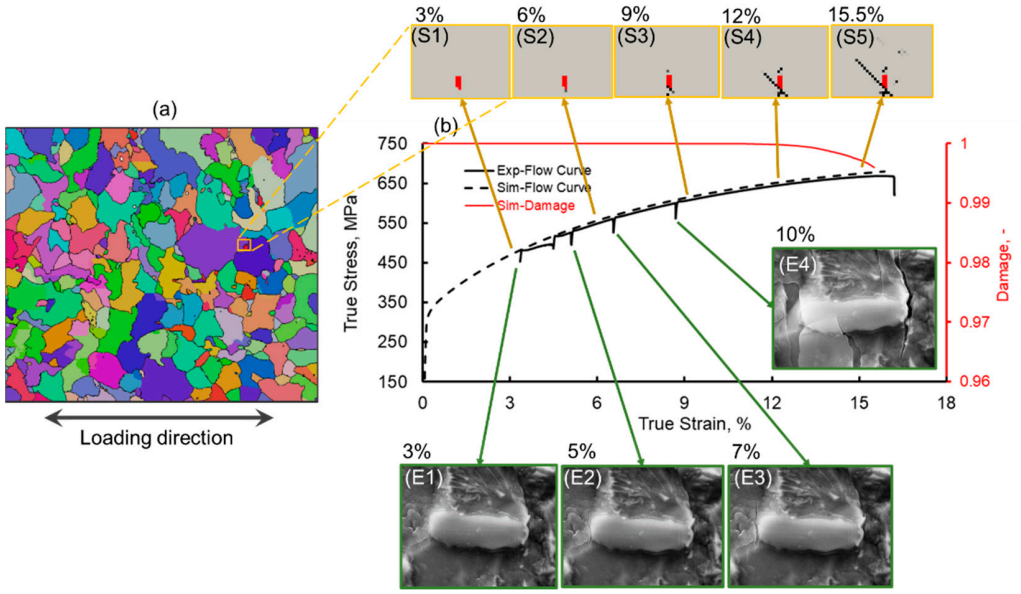

Figure 8. (**a**) RVE chosen to run full phase simulations in IPF colors; yellow box represents one of the crack initiation zones. (**b**) Outcome of the simulation flow curve in comparison with the in situ experimental test results, showing a good match; the dips in the experimental results are the points where the test was stopped to take local pictures of the inclusions for later DIC. E1–E4 show the damage evolution around an MnS inclusion, S1–S5 inset figures show the damage evolution around a comparable MnS inclusion during numerical simulation.

A good correlation between global experimental and numerical simulation results is observed with less than 3% difference of predictions. The inset figures in Figure 8 from S1–S5 show damage evolution around an MnS inclusion. Inset figures E1–E4 show damage evolution around a similar-sized MnS inclusion captured during in situ testing. Interestingly, not only do the global results match well, but the local damage evolution is also comparable. These local deformation and damage trends are discussed later in this article.

4.2. Local Results of Numerical Simulation

The local distributions of strains, stress, triaxiality, and damage at 3%, 9%, and 15.5% of global strain are shown in Figure 9. Due to the heterogeneous distribution of non-metallic inclusions and different Schmidt factors of each ferrite grain, the local distributions of each attribute are largely heterogeneous. Therefore, the grain boundaries have been overlaid in contrasting colors to clarify the distributions of attributes within individual grains.

It is observed that at 3% global strain, the local strain distribution is relatively homogeneous within the selected RVE. As the global strain increases and reaches a maximum of 15.5%, an extreme heterogeneous distribution of strain along the grain boundaries in thick channels aligned at 45 degrees to the loading axis is observed with intermediate areas of very low local strain. On the other hand, the stress distribution is high from the beginning in the ferrite grains with a high Schmidt factor and increases significantly within those grains. The value remains similar as the global strain reaches the maximum value.

Of course, the local stress and strain distribution is largely affected by the presence and distribution of non-metallic inclusions. The behavior is discussed in more detail in the next section.

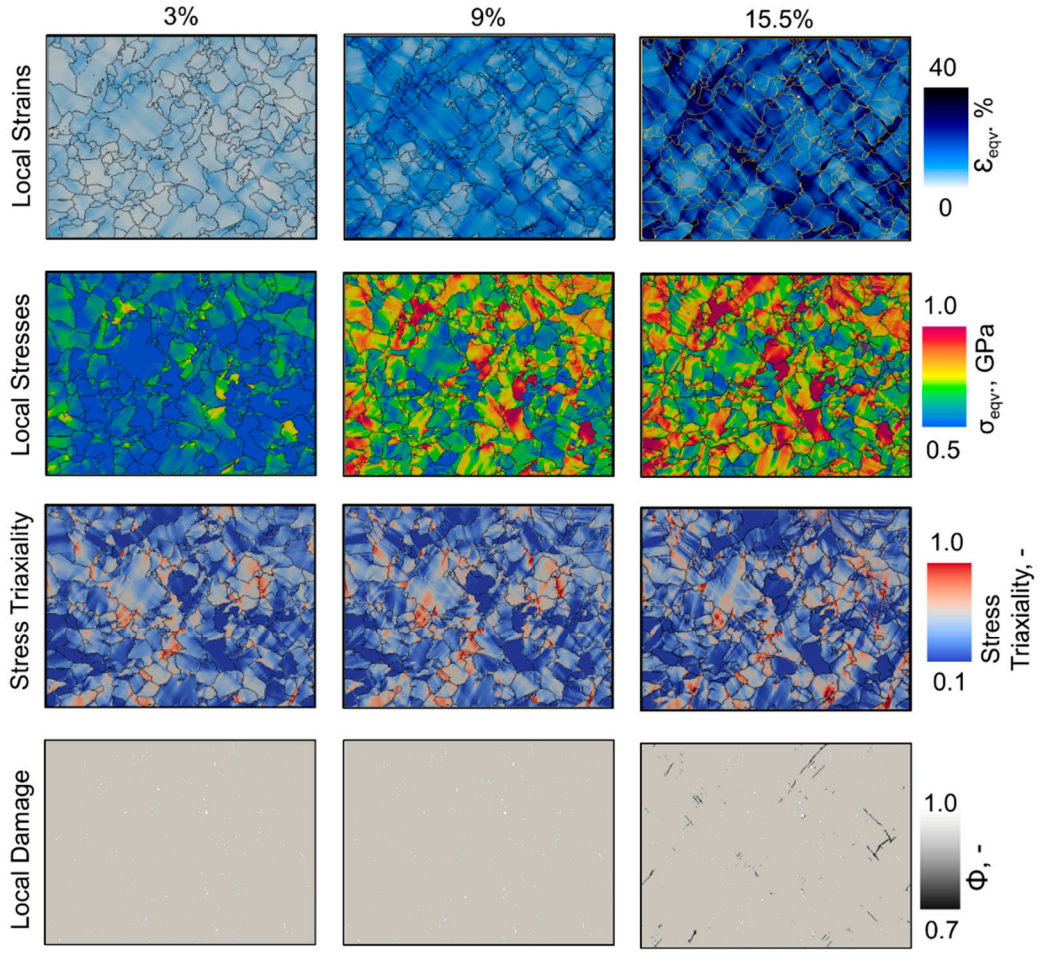

Figure 9. Evolution of local strain, local stress, stress triaxiality, and local damage in the selected RVE at 3%, 9%, and 15.5% global true strains, where the loading axis is horizontal to the micrographs.

Stress triaxiality is the relative degree of hydrostatic stress in each stress state, which is usually used to estimate the type of fracture that might take place in the material. In the current RVE, it is observed that the triaxiality measure in most of the grains is close to 0.1, which means that the stress (no matter how high) is predominantly hydrostatic. Therefore, the deviatoric component of stress in these grains is low and will not contribute significantly towards material flow and eventual damage. In addition, it is interesting to note that the triaxial stress remains consistent with the increase in strain and only slightly shifts to neighboring grains after the damage initiation and propagation.

Generally, it is observed that the damage initiates at the interface of the non-metallic inclusions, especially in the narrow zones locked between the cluster of inclusions. After initiations, the damage propagates at an oblique angle to the applied external load. As a result, the local voids coalesce and form larger cracks that grow faster, and material damage accelerates. It is important to mention here that the continuum mechanics simulations are intrinsically unstable due to the loss of stiffness at several solution points. Furthermore, it takes immense computing power to calculate the corresponding equilibrium for each increment after damage initiates in the RVE. Therefore, the simulations were only computed up to 15.5% of the global strain, and the results are shown in Figure 9.

Although the local results generally for the ferrite matrix are shown in Figure 9, one of the main objectives of this article is to investigate the effect of non-metallic inclusions

on the material's local deformation and damage behavior. In Figure 10, the focus has specifically been shifted towards three different zones in the RVE of comparable size with different inclusion compositions and distributions. Zone-I comprises a single grain with a large MnS inclusion in the middle. Zone-II comprises several small ferrite grains with a clustered distribution of non-metallic inclusions primarily on the grain boundaries. Zone-III comprises relatively larger ferrite grains with a diffused distribution of non-metallic inclusions within the grains and on the grain boundaries. The distribution of local attributes in the three zones is selectively identified in the corresponding subplots Figure 10b–e. There is a relatively low stress concentration in zone-I and less strain due to almost nonexistent stress triaxiality, and therefore, no damage takes place in this zone. This can be due to the high Schmidt factor of this specific grain and the central position of a large hard MnS inclusion which restricts the slip planes from moving in this grain freely.

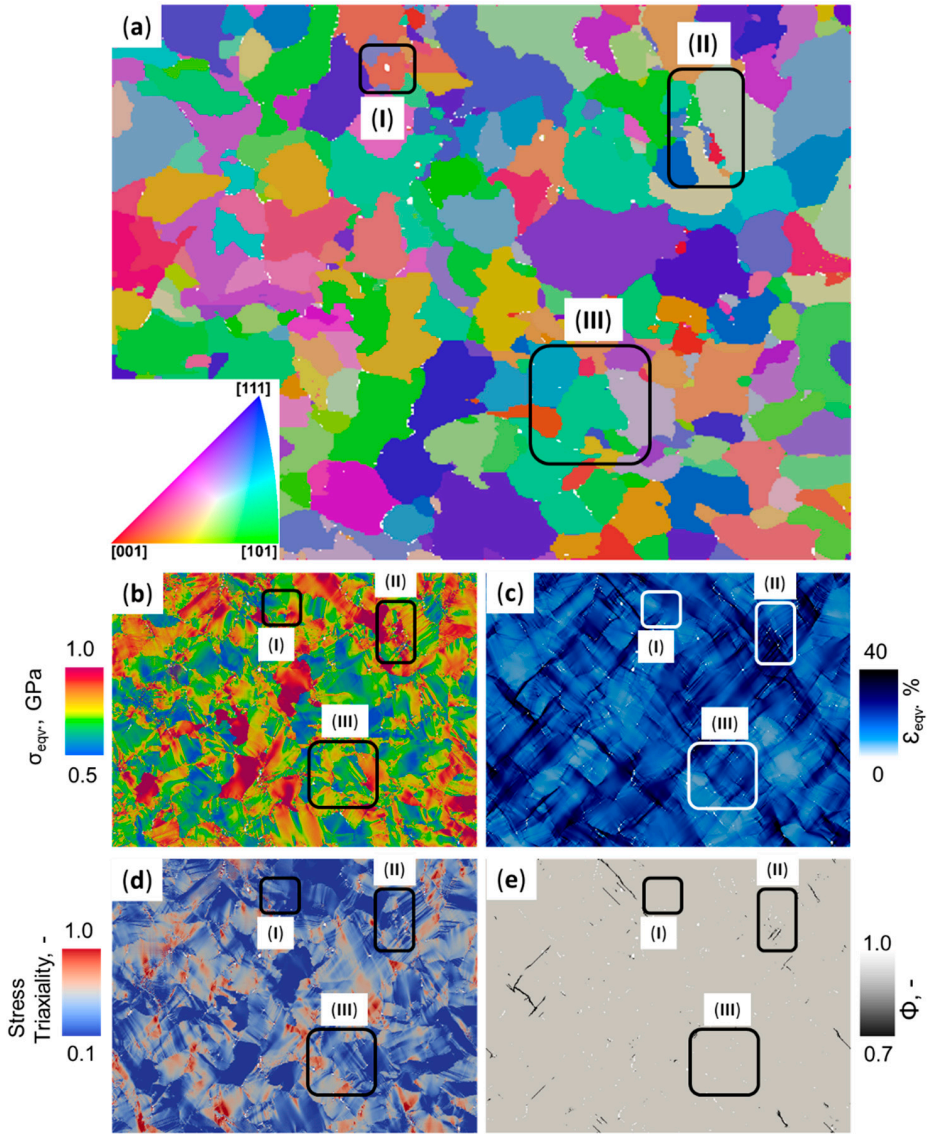

Figure 10. A construction figure with (**a**) showing the selected RVE with the identification of three zones. All non-metallic inclusions are displayed by white points. In other subplots, (**b**) true Mises stress, (**c**) true Mises strain, (**d**) stress triaxiality, and (**e**) damage propagation withing the ferrite matrix are shown. Zone-I has a ferrite grain with a large MnS inclusion in the middle, zone-II is a region of small ferrite grains with clustered non-metallic inclusions present on the grain boundaries, and zone-III has relatively large ferrite grains with a dispersed distribution of non-metallic inclusions within grains and on the grain boundaries. The loading axis is horizontal to the micrographs.

Small non-metallic inclusions distributed on the grain boundaries of small ferrite grains act as high-stress concentration sites with the large plastic flow in zone-II. Consequently, the stress triaxiality in this zone is relatively high, indicating a large plastic flow and evolution of ductile damage. This damage evolution due to the coalescence of small voids that form on the inclusion/matrix interface is visible in Figure 10e. It is observed that local damage incidents join together to form microcracks that propagate at maximum shear plane oriented 45 degrees to the loading axis. This can be due to two reasons: first, due to the 2D nature of the RVE, as has been pointed out in the previous work [52]; and second, due to the high amount of slip system activation in grains and areas with maximum critical resolved shear.

Zone-III comprises relatively larger ferrite grains with a relatively broader distribution of non-metallic inclusions within the grain and grain boundaries. In zone-III, although the triaxiality is comparable with zone-II, due to the lack of clustering on non-metallic inclusions, the stress distribution and strain distribution are lower. Hence, no damage occurs in the zone.

In Figure 10, a qualitative comparison of local attributes in three different zones shows how the distribution of non-metallic inclusions plays a role in affecting the local stress, strain, and damage. To quantitively compare three zones, a statistical normalized probability distribution was adopted to systematically compare the distribution of stress and strain within zone-I, zone-II, and zone-III, as shown in Figure 11.

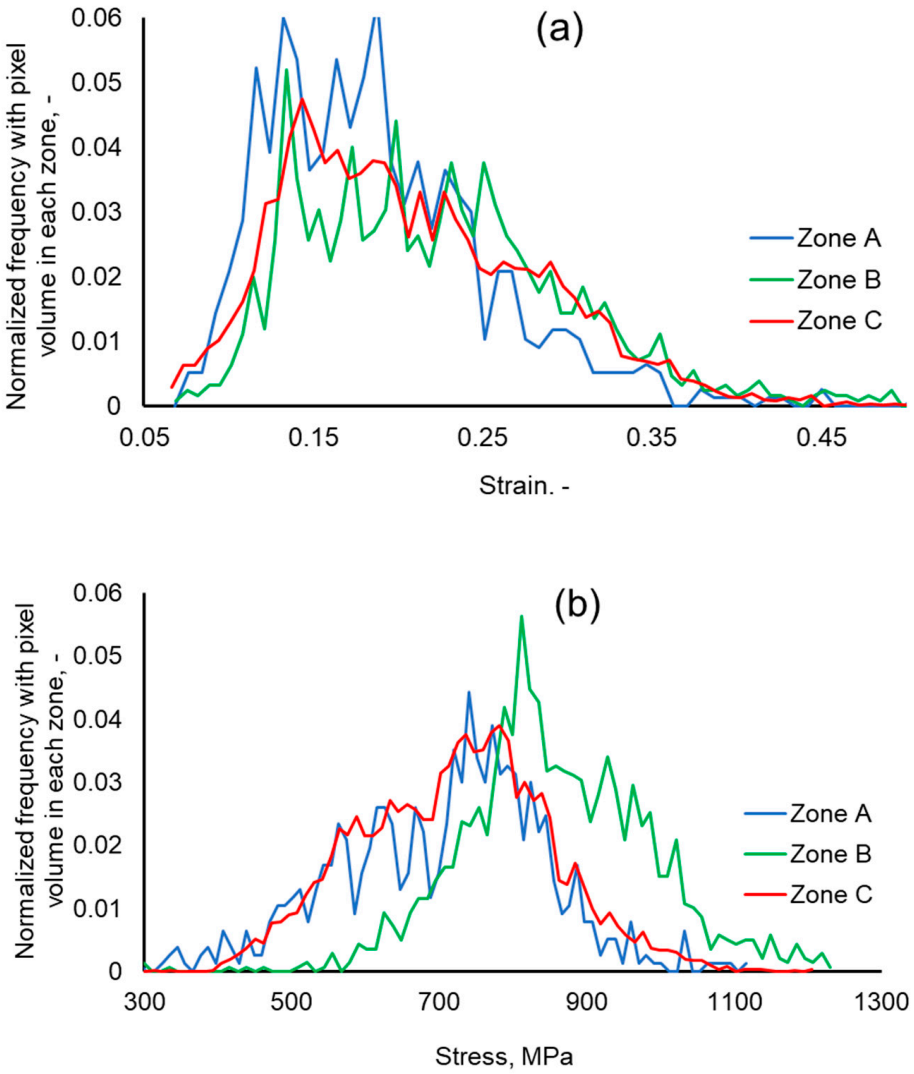

Figure 11. The normalized frequency of (**a**) strain and (**b**) stress for each zone identified in Figure 10.

To quantitatively compare the stress and strain distribution in zones I to III, a statistical distribution tool is used, and the results are presented in Figure 11. It is observed that the strain distribution in all three zones, as shown in Figure 11a, is very similar. It peaks around 0.15–0.18 and then linearly drops to a strain of 0.45. The strain in zone-I is slightly higher and that in zone-II is slightly lower due to the local orientation distribution. The stress distributions in these zones reach up to 1100 MPa.

The statistical stress distribution in the three zones is presented in Figure 11b and proves the already stated hypothesis. It is observed that the stress in zone-I and zone-III peaks around 750 MPa, with a slight bias towards the lower stress side. On the other hand, the stress distribution in zone-II, due to the close clustering of several non-metallic inclusions on the grain boundaries of small ferrite grains, peaks at 850 MPa (11% higher than the other zones), and its distribution is biased towards the higher-stress side. The distribution reaches 1250 MPa (12% higher than the other zones). This high local attribute distribution in zone-II makes it more prone to local damage initiation and propagation in high deformation regimes.

4.3. Local Results of the In Situ Tensile Test

The local results of the in situ tensile tests at 3%, 5%, and 8% of global strain are shown in Figure 12 The methodology and procedure of local strain measurement is provided in Appendix B. The complete set of results, due to its extensiveness, is provided in Appendix C of this article. Readers can refer to Appendix B and C for further details about collection and frame by frame evolution of local strain measurements.

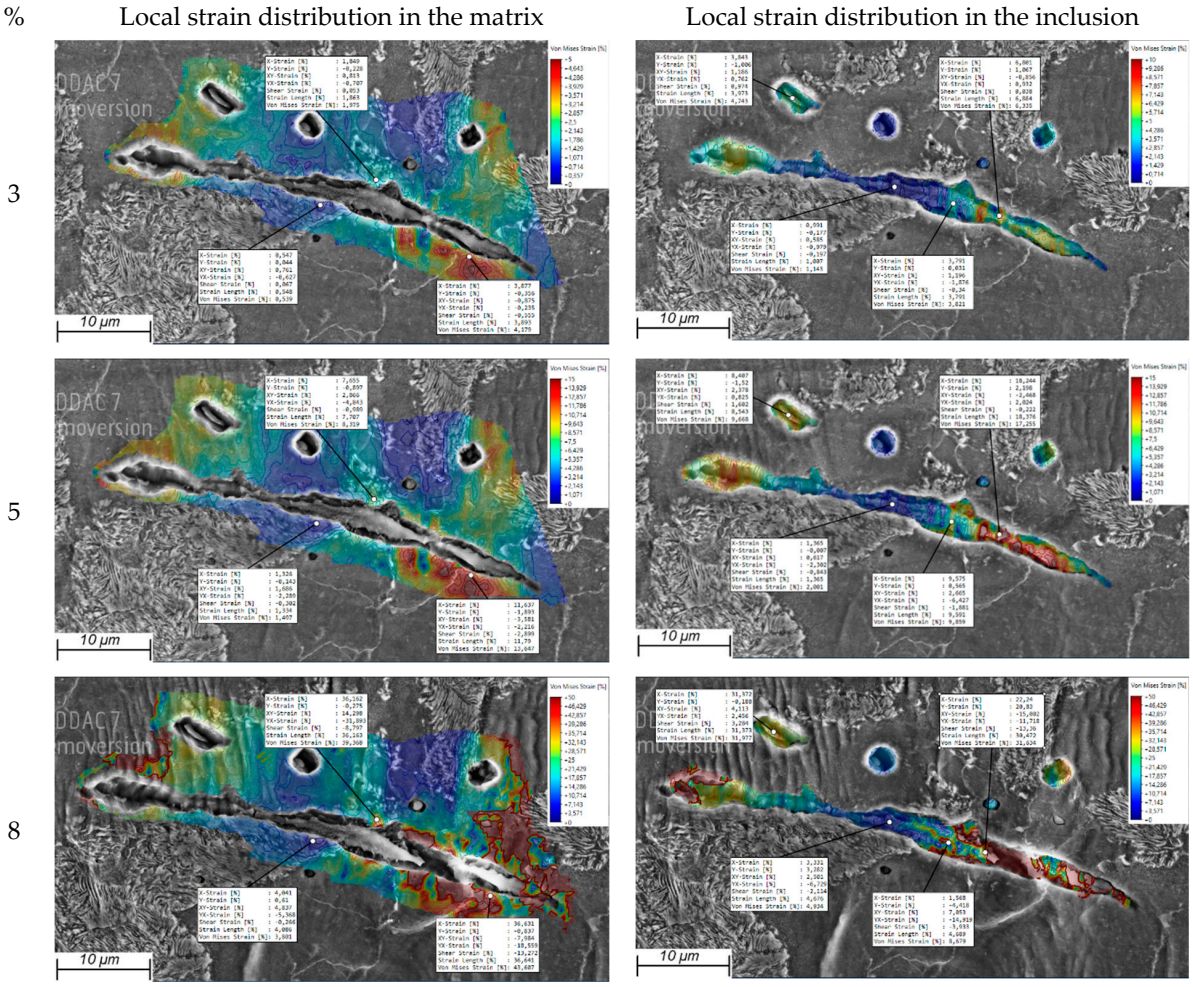

Figure 12. Local strain distribution in ferrite matrix and MnS inclusion at 3%, 5.5%, and 8% global strains.

In Figure 12, at a subsequent global strain of 3% and 400 MPa global stress, it can be observed that in the zones with increased elongation, the strain rate is much higher than in the zones where the strain rate has not increased much from the beginning of the test. The effect of the increase in elongation at the ferrite grain boundaries near the non-metallic inclusion is preserved. At this stress, two zones with a significant increase in strain can be seen in the middle of the inclusion. When comparing the entire image series, at a load of 450 MPa and global strain of 5%, the sulfide inclusion is cracked in the area of thinning. The inclusion in the left part of the crack is brighter due to its change in position, which significantly affects the strain values in this inclusion area, as the digital image correction software requires areas with contrast for accurate calculation. The breaking point itself is hidden at this point due to the topography.

The maximum values in the range of increased load are above 8.9%. It is observed that the two sulfide inclusions move further away from each other. The strain in the region increases, reaching a value of over 13–64%. Around the formed cavity of a small inclusion located on the upper right side of the elongated inclusion, the elongation near the pearlitic zone is greater than on the other side of the same grain. On the side of the ferrite grain around this cavity is a zone of increased deformation with a value of about 7–11%. There is a significant difference in elongation within and around the small cavities. In the middle cavity, the deformation is minimal and is between 2% and 3.5%, while in the left cavity, the deformation around and within the cavity is between 6.4% and 9.8%.

Due to further load increase and subsequent high strain values, the DIC program loses previously captured pixels for the calculation. By enlarging the gaps created, some pixels can significantly change their gray tone, causing the program to find a similar range of pixels elsewhere and greatly distorting the calculation values. At a maximum global strain of 8% (450 MPa), a large loss of pixels is observed (in areas beyond the specified deformation limit of dark red) because the topography changes too much, and the color range continues to change in many areas. In addition, the distance between the halves of the sulfide inclusion become significantly large. In the lower deformation zone in the matrix around the sulfide grain inclusion, the values are 43.6%. In contrast, the zone-I around the inclusion next to the perlite grain remains below the total deformation.

4.4. Damage Evolution around Non-Metallic Inclusions

The MnS inclusion tracked to analyze local deformation and damage behavior in Figure 12 is an exception. Usually, the inclusion size in the material user consideration is between 1–4 μm; please refer to Figure 4 for reference. Unfortunately, such small inclusions are hard to track and record local strain around due to high magnification, resulting in fast drifting during testing in the SEM chamber [53]. Despite this paradox, in the current work, during in situ testing, a few MnS inclusions of small size were tracked and recorded at different strains. The results are shown in Figures 13 and 14.

In Figures 13 and 14, several inclusions classified as MnS inclusions based on the EDS analysis were tracked at different external strains that were applied. The results shown here were at the beginning of the test when the inclusions were identified, at external load when the damage was initiated, and an external load when the damage started to evolve.

In Figure 13, it is observed that the damage initiates perpendicular to the line of action of the load at about 525 MPa global stress and propagates in that same direction. It is important to keep in mind that the inclusion is embedded in the matrix, and here only the surface is being observed. The surface matrix seems to be extremely deformed due to the internal propagation of the damage around the inclusion. It is also interesting to note that the damage initiates at the inclusion/matrix interface. In contrast, the inclusion remains free of any cracking, unlike the case of large inclusion, which was shown and discussed earlier in Figures 5 and 12. This is because the damage of the inclusion is a function of the size and distribution in the matrix, where small inclusions with an aspect ratio of less than 2.5 are generally not highly prone to damage.

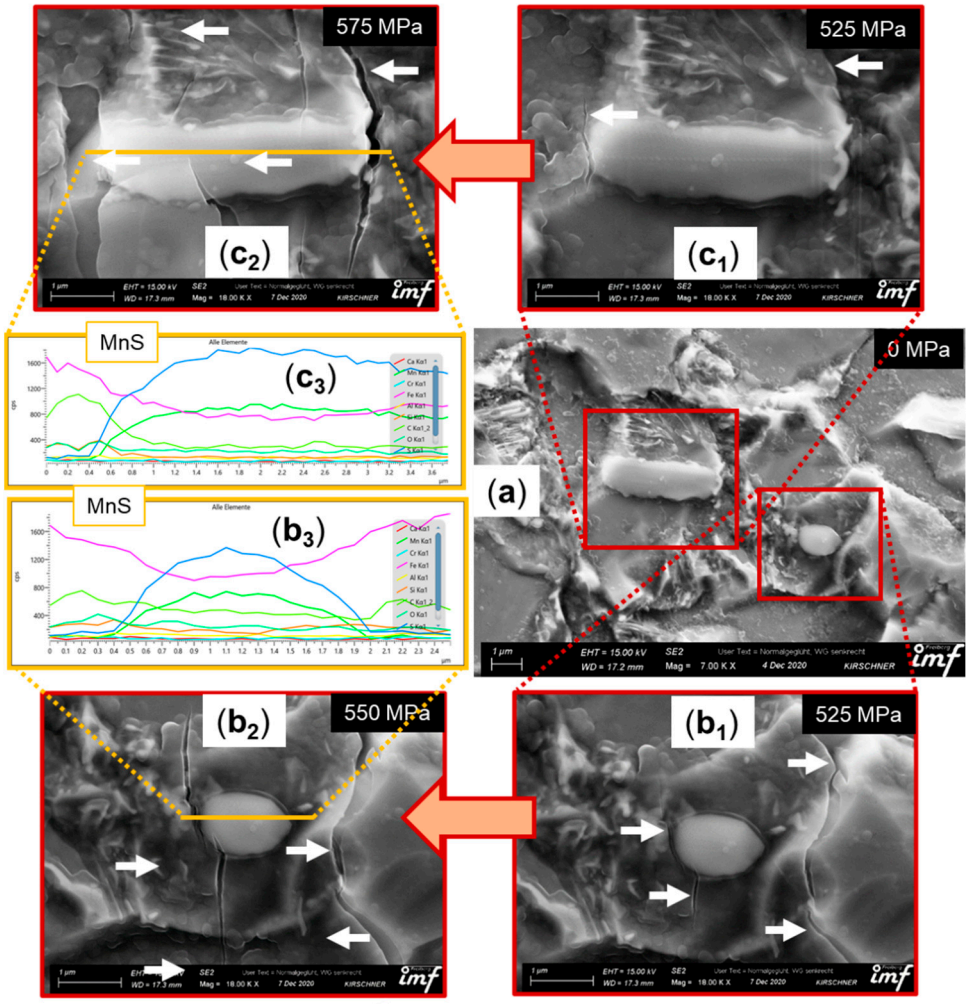

Figure 13. (**a**) Localized single inclusion identification, (**b**) represents a round inclusion at 525 MPa and 550 MPa, respectively. (**c**) represents an elliptical inclusion at 525 MPa and 550 MPa, respectively. EDS show the maximum concentration of manganese and sulfur along the measured length verifying both to be an MnS inclusions. The white arrows point to the local damage initiation and growth.

In Figure 14, two other inclusions are tracked, again identified as MnS based on the EDS analysis shown in the same figure. Both inclusions are completely embedded in small ferrite grains and resemble the case of zone-I in Figure 10.

In Figure 14, it is observed that the damage starts to initiate at 550 MPa of external load, which is slightly higher than the damage initiation load for other inclusions but is in a similar range. At 575 MPa of external load, damage on the inclusion matrix interface grows so extensive that it is easily identifiable and is marked with the help of white arrows. In this case, it is observed that voids initiate at an oblique angle to the applied external load and not perpendicular to the load as observed earlier. This position of the damage initiation depends on several factors: i.e., orientation, size, shape, and sharpness of the inclusion edges and the place of the inclusion (inside a large grain or on the grain boundary). It would also largely depend on the orientation of the surrounding matrix grains. As mentioned earlier, all these inclusions have 3D geometry, and the third dimension would also affect the results observed on the surface of the specimen.

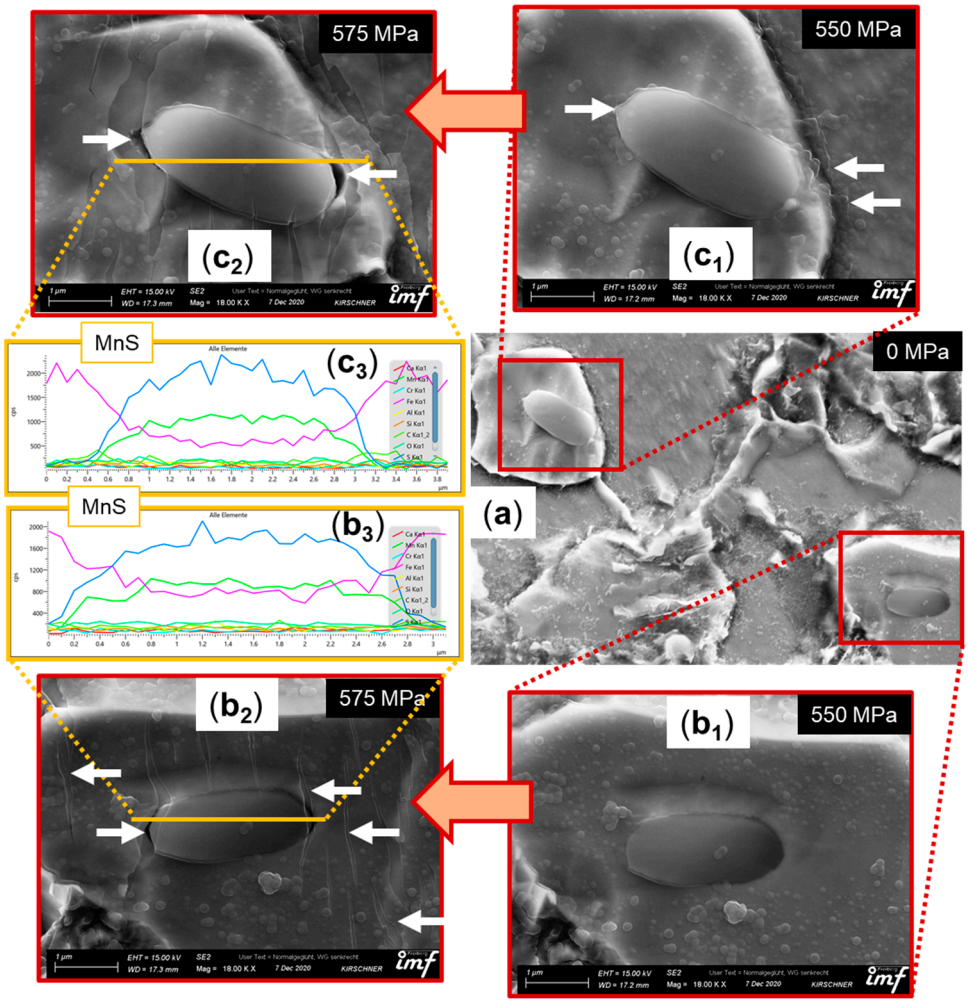

Figure 14. (**a**) Localized single inclusion identification, (**b**) represents an elliptical inclusion parallel to the applied load at 550 MPa and 575 MPa, respectively. (**c**) represents an elliptical inclusion placed 30 degree to the applied load at 550 MPa and 575 MPa, respectively. EDS show the maximum concentration of manganese and sulfur along the measured length verifying both to be an MnS inclusions. The white arrows point to the local damage initiation and growth.

5. Discussion

The global and local deformation and damage behavior of modified 16MnCrS5 steel (composition in Table 1) is analyzed. Before the in situ testing, the specimens were prepared using a special grinding and polishing technique (presented in detail in Appendix A), and detailed EBSD data were collected to understand the morphology of the matrix and the second phase inclusions. The outcome of the statistical analysis of the collected microstructural data is presented in Figures 3 and 4. It is evident that, generally, the non-metallic inclusions are quite small, and the MnS inclusions are slightly larger and more visible at the set magnification. Although the MnS inclusions were the focus of this work, other inclusions are also expected to behave similarly.

The parameters of the crystal plasticity model were calibrated and then incorporated in the full phase model employing the recorded and cleaned EBSD data. It is observed that the global results of the simulation match well with the experimental observations. Therefore, researchers can successfully use the identified parameters to model this material using DAMASK in the future. However, one can argue that this match of global results is because a similar data set was used to calibrate these parameters. To answer that critique, the damage pattern around a comparable inclusion in experiments and simulations was made at different strains, and a remarkable similarity in the trends was observed.

Apart from the global results, the local simulation results provide great insight into how the inclusion size, position within the matrix, and their distribution affect the local stress, strain, damage, and triaxiality. The trends of local strain distribution match well with the previously published data [28,54]. A qualitative and quantitative comparison of the three different zones was presented in Section 4.2. All three zones are intrinsically different based on the composition, inclusion size, and distribution. In addition, there is a clear difference in the damage behavior in these zones, and local stress distribution is observed. These local attributes account for the different local material behavior observed in the experimental part of this work.

Since the previous works have shown that the second phase inclusions are major players in defining the formability of the material [15,41,55], a special focus was given to them in this work. Previous work [51–56] shows that the morphology and distribution of the second phase inclusions dictate the formability limit and damage degradation in a material. In this work, in situ tests were carried out focusing on the strain evolution and damage evolution around and within these second phase inclusions. The second phase inclusion size distribution is observed to be close to 1 µm with a few larger inclusions in the specimen. The local strain around and within one of these exceptionally large MnS inclusions is studied in detail. MnS inclusions, due to their larger size, are easily identifiable at the magnification range selected in this study, and therefore they appear predominantly in this work. However, it is assumed that other inclusions behave similarly. This is also verified by the simulation results presented in Section 4.2, where all the inclusions behave almost indifferently under applied external load.

The results of the local strain measurement from the in situ tests are presented in Section 4.3. It is observed that the strain in the matrix is higher at some points and lower at some points, depending on the orientation of the corresponding ferrite grain. The inclusion is observed to have a low strain distribution until a brittle fracture appears, which damages the whole microstructure, and it becomes hard to track the local strain in the material further. Small MnS inclusions were also tracked in this work at increasing external loads. For these smaller inclusions, it is observed that matrix/inclusion interface decohesion starts to take place and grow at high strain regimes of >550 MPa. These findings match well with the previously published work of other researchers [4,6,19,44,56].

Although similar research with in situ tests and crystal plasticity simulations has been previously carried out by some researchers before [21,27,28,57,58], it was either pure simulation or pure experimental work. No correlation using both methods has been presented before concerning how the inclusion distribution, size, and morphology affect the material deformation and degradation. However, in this work, the findings of the developed crystal plasticity-based numerical simulation model have been validated. Researchers and industry can now use this tool to analyze and optimize the non-metallic inclusion size, distribution, and morphology to attain the desired material formability.

6. Conclusions

The global and local deformation and damage behavior of modified 16MnCrS5 steel using in situ experimental and crystal plasticity-based numerical simulation model is analyzed. Recorded EBSD data were used to evaluate the local microstructure of the material. The data were then adopted to run full phase crystal plasticity simulations in DAMASK with calibrated material model parameters. In situ tensile tests were carried out on specially prepared specimens with incremental data collection for different inclusions distributed within the ferrite matrix. A images were processed using digital image correlation-based tool to obtain microstrain measurements. The damage initiation, propagation, and strain localization around a large MnS inclusion were analyzed in detail. Other smaller inclusions tracked in this study helped in understanding the local material behavior. The conclusions of this extensive study are as follows:

1. The non-metallic inclusions are heterogeneously sized and heterogeneously distributed within the ferrite matrix. The inclusions are usually small (size ~2 µm)

and elliptical (aspect ratio < ~2), with the exceptions of some extremely large (>10 μm up to 50 μm) and elongated (aspect ratio > 5) inclusions that are also present in the matrix. These large and elongated inclusions play a critical role in defining the limiting formability of the steel under consideration.

2. The 2D full phase simulation model developed in the current work provides accurate information about the material's local damage initiation and propagation under consideration. Although the same areas were not compared quantitatively, the simulation results match the experimental observations of global stress–strain response and the local damage initiation around the inclusions. Hence, the model can be used by engineers and researchers for further material engineering and optimization with confidence.
3. The local stress and strain largely depend on the local composition and distribution of non-metallic inclusions and the size and orientation of the neighboring ferrite grains. The local stress in highly clustered zones is ~12% higher than the other material zones where the inclusions are more dispersed within the matrix.
4. The damage initiation and propagation also depend on the inclusion size and position. If the inclusion is very large, brittle fracture occurs at relatively lower applied external stress (~450 MPa), which results in the fast damage initiation and propagation in the matrix. For most small and relatively elliptical inclusions, the damage initiates on the matrix/inclusion interface at relatively high-stress regimes (~550 MPa). It propagates at an oblique angle to the applied load. These smaller and relatively elliptical inclusions are also less prone to brittle cracking and strengthen the matrix during deformation.
5. An adequate material manufacturing methodology should be employed for the material class under consideration, resulting in small, elliptical, homogeneously distributed inclusions within the ferrite matrix. This would result in a material with better formability and higher damage resistance.

Author Contributions: Conceptualization, F.Q. and M.U.; methodology, F.Q. and M.U.; software, F.Q. and M.U.; validation, F.Q., V.E., M.K. and S.G.; formal analysis, F.Q., M.U., V.E. and F.H.; investigation, V.E., M.K., F.H. and S.G.; resources, F.Q., V.E., M.K. and S.G.; data curation, F.Q. and M.U.; writing—original draft preparation, F.Q., M.U. and S.G.; writing—review and editing, F.Q., M.U., S.G. and U.P.; visualization, F.Q., M.U., S.G. and U.P.; supervision, U.P. and S.G.; project administration, S.G. and U.P.; funding acquisition, F.Q., S.G. and U.P. All authors have read and agreed to the published version of the manuscript.

Funding: This research was funded by Industrielle Gemeinschafts-Forschung (IGF) under project number 20429 BG, titled "Nichtmetallische Einschlüsse".

Institutional Review Board Statement: Not applicable.

Informed Consent Statement: Not applicable.

Data Availability Statement: The data are not publicly available but can be shared with interested researchers privately upon request.

Acknowledgments: The authors acknowledge the DAAD Faculty Development for Candidates (Balochistan), 2016 (57245990)-HRDI-UESTP's/UET's funding scheme in cooperation with the Higher Education Commission of Pakistan (HEC) for sponsoring the stay of Faisal Qayyum at IMF TU Freiberg. This work is conducted within the DFG-funded collaborative research group TRIP Matrix Composites (SFB 799). The authors gratefully acknowledge the German Research Foundation (DFG) for the financial support of the SFB 799. The authors also acknowledge the support of Martin Diehl and Franz Roters (MPIE, Düsseldorf) for their help regarding the functionality of DAMASK.

Conflicts of Interest: The authors declare no conflict of interest.

Nomenclature

Acronyms

Symbol	*Description*
SEM	Scanning electron microscope
SE	Secondary electron (detector)
BSE	Back scatter electron (detector)
EDS	Eenergy dispersive spectorscope
EBSD	Electron back scatter diffraction
DAMASK	Düsseldorf advanced material simulation kit
RVE	Representative volume element
NME	Non-metallic inclusions

Appendix A. Limitations and Challenges Associated with the In Situ Tensile Test Methodology

Before the in situ tensile tests, the specimens were metallographically polished (OPS). Since the deformed surface of the test specimens was later to be analyzed with digital image correlation software, the test specimens were etched for 5 s in a 3% Nital solution to achieve the required surface contrast. The experiment revealed that only non-deformed inclusions were found on the surface of the specimens, while non-metallic sulfide inclusions with an elongated shape were in the middle of the specimens examined. For further tests, the specimens were ground to a thickness of 0.6 mm and then polished and etched. Since the specimens were very thin, manual grinding was not possible because it was not possible to avoid deviations in the thickness of the specimens. A conventional embedding mass was not suitable for specimen preparation because there was a high risk of damaging the specimens when detached from the embedding mass therefore It was decided to use the embedding mass Technovit-5071 as shown in Figure A1. A special feature of this embedding mass was that the specimens could be dissolved after processing by dissolving the embedding mass in acetone when heated to 30 °C.

Figure A1. Specimens after polishing in Technovit-5071.

Within the scope of this work, an attempt was made to generate a special pattern [7] on the specimen surface for the digital image correlation program with the help of polystyrene latex beads with a diameter of 0.095 µm. However, due to the previous etching, it was difficult to achieve an even distribution on the surface, as all the beads accumulated in the

resulting depressions (Figure A2). The available DIC systems, such as VEDDAC, GOM, and VIC-2D, have therefore not made a flat closed evaluation possible. Therefore, the procedure with balls was not pursued in further investigations. The focus was placed on a special etching of the specimen surface with the application of the "InLens" module.

The method for the deposition of SiO_2 nanoparticles on the specimen surface was as follows:

1. The surface of the specimen was metallographically prepared for colloidal silicon dioxide (OPS);
2. On a clean polished dip plate, 10–20 drops of OPS were placed along the diameters;
3. The specimen was pressed onto the cloth with 1–2 MPa pressure and turned for 1 s at 2 rpm;
4. With water flushing and 100 RPS plate speed, the specimen was rotated on the cloth at 1–2 MPa pressure at 2 RPS for 3 s;
5. The specimen surface was rinsed with ethanol and dried with a blower.

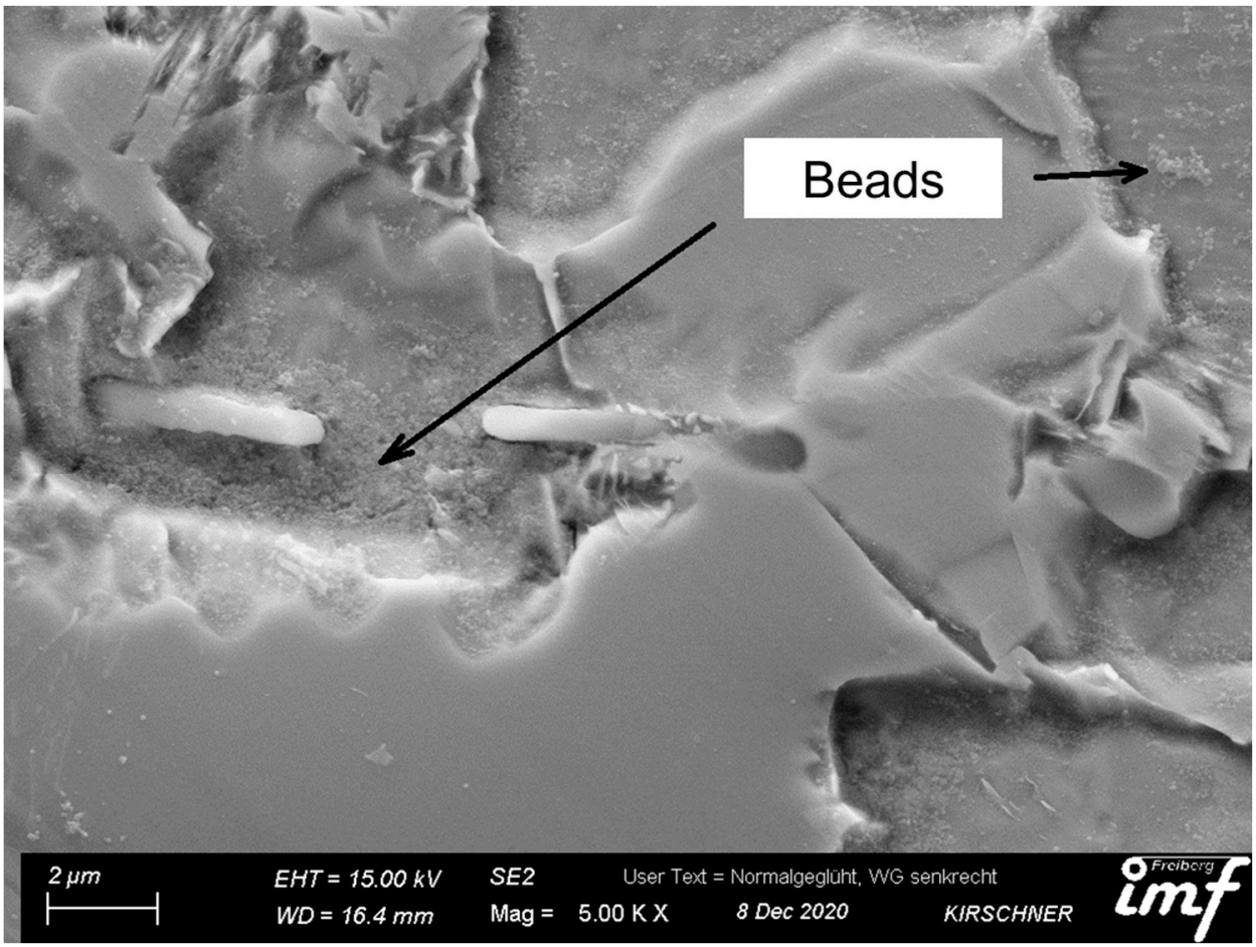

Figure A2. Example of the accumulation of polystyrene latex beads in the deep spots created by etching.

As part of this work, various tests were also carried out to create contrasts on the surface of the specimens. To achieve the desired contrast, different etching times of 2 to 15 s were used (Figure A3).

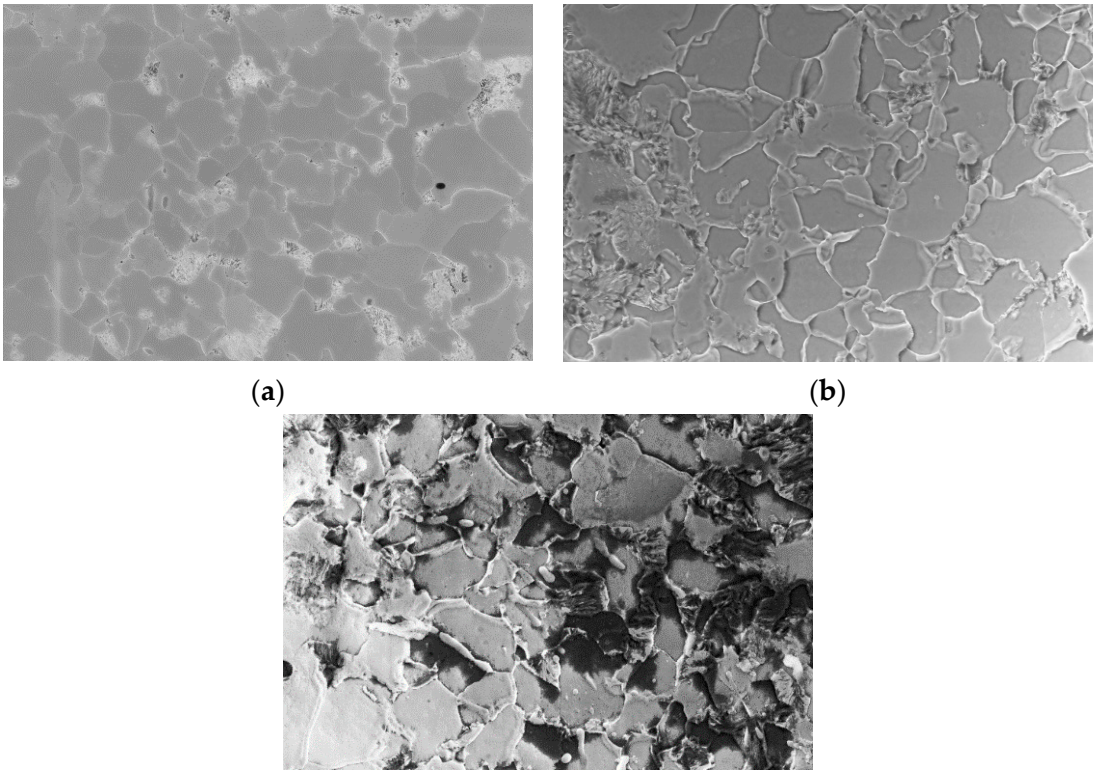

(**a**) (**b**)

(**c**)

Figure A3. Example of a microstructure surface with different etching times: (**a**) 2 s, (**b**) 5 s, (**c**) 15 s.

Various scanning electron microscope modules such as SE (Figure A4a) and "InLens" (Figure A4b) were used.

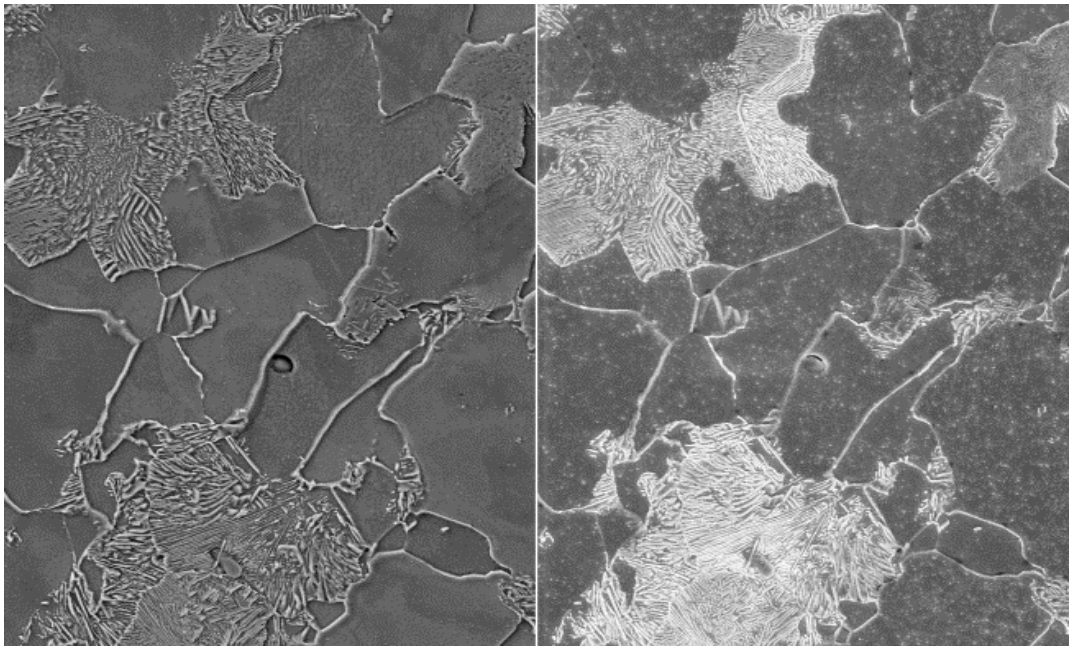

(**a**) (**b**)

Figure A4. Example of a microstructure surface using different modules: (**a**) SE, (**b**) "InLens".

Different contrast values were used in the settings of the electron beam microscope (Figure A5a contrast = 49%, Figure A5b contrast = 52%).

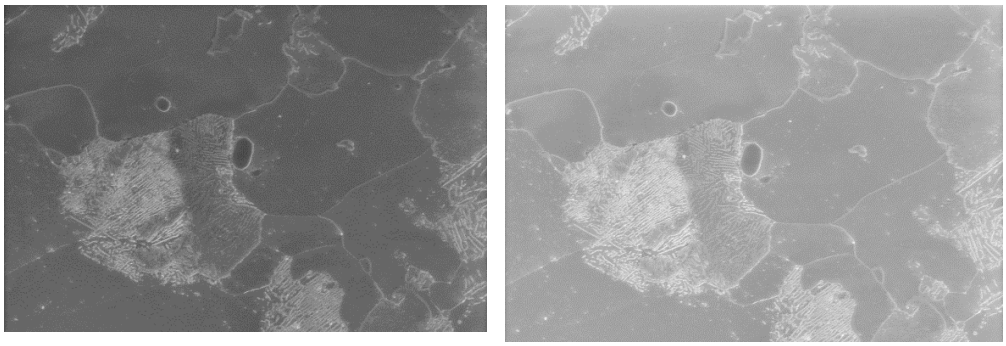

(**a**) (**b**)

Figure A5. Example of a microstructure surface at different contrasts of SEM: (**a**) contrast = 49%, (**b**) contrast = 52%.

Appendix B. Local Mises Strain Measurement

The von Mises strain at the meso plane was calculated using a scale in the areas studied (Figure A6). On each surface of the undeformed specimen, three points were selected so that one point was common; they formed two identical straights, and there was an angle of 90° between these straights.

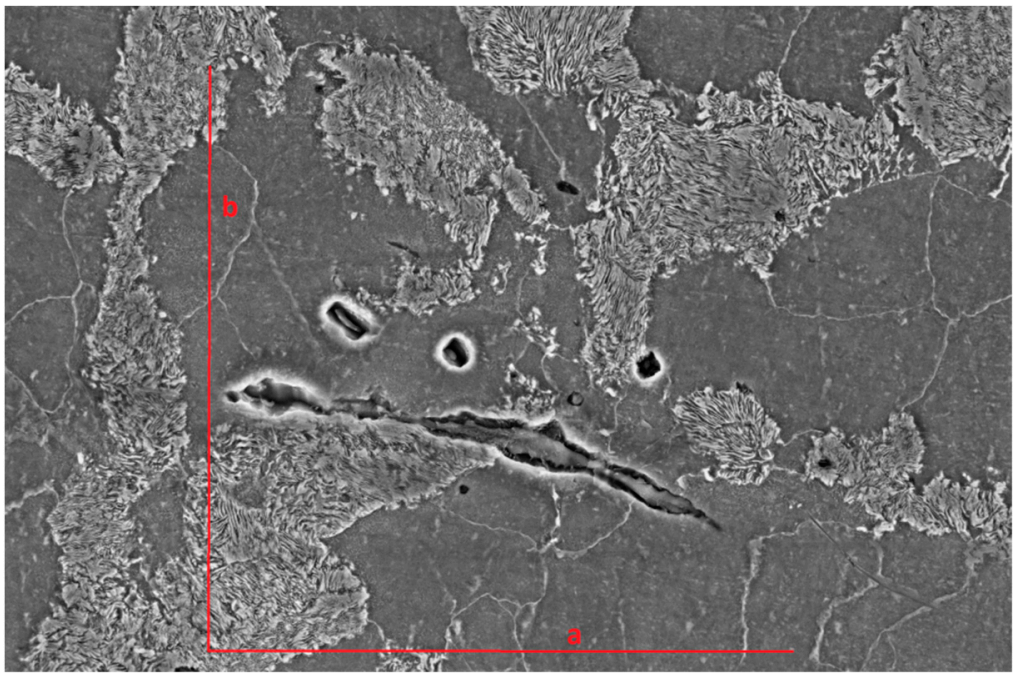

Figure A6. Account length of the selected area used to calculate mesoscale plane-strain for the tensile specimen (11K).

The strain was calculated using the following formula:

$$\varnothing_1 = ln\frac{a}{a_0} = \frac{1}{2}ln\frac{a_1^2 + b_1^2 + \sqrt{\left(a_1^2 + b_1^2\right)^2 - 4a_1^2b_1^2sin^2\delta}}{2a_0^2} \quad \text{(A1)}$$

$$\varnothing_2 = ln\frac{a}{a_0} = \frac{1}{2}ln\frac{a_1^2 + b_1^2 + \sqrt{\left(a_1^2 + b_1^2\right)^2 - 4a_1^2b_1^2sin^2\delta}}{2a_0^2} \quad \text{(A2)}$$

$$\varnothing_v = \frac{2}{\sqrt{3}}\sqrt{\varnothing_1^2 + \varnothing_2^2 + \varnothing_1\varnothing_2} \quad \text{(A3)}$$

As a result of the tests, the meso deformation in the long inclusion in the tensile specimen was calculated. The results of meso-scale deformation are presented in Table A1.

Table A1. Change in the length of the account of the selected area and angle at the meso plane for the tensile specimen.

MPa	A [μm]	B [μm]	Angle of Axis A [Degrees]	Angle of Axis B [Degrees]	Angle [Degree]
0	50	50	0	90	90
300	50.63	49.87	0.5	90	89.5
375	50.8	49.96	0.1	90.1	90
400	51.1	49.83	−0.19	90.4	90.59
425	51.52	49.66	−0.28	90.24	90.52
437	51.94	49.66	−0.37	90.19	90.56
450	52.41	49.62	−0.42	90.44	90.86
462	53.46	49.54	−0.54	90.73	91.27
450_2	57.01	49.89	−0.72	91.5	92.22

The tests yielded the stress–strain diagram shown in Figure A7. The diagram shows that the range of plastic deformation started at 300 MPa. The maximum tensile strength achieved was 462 Mpa, and the breakage of the specimen began at a stretch of 7.9%

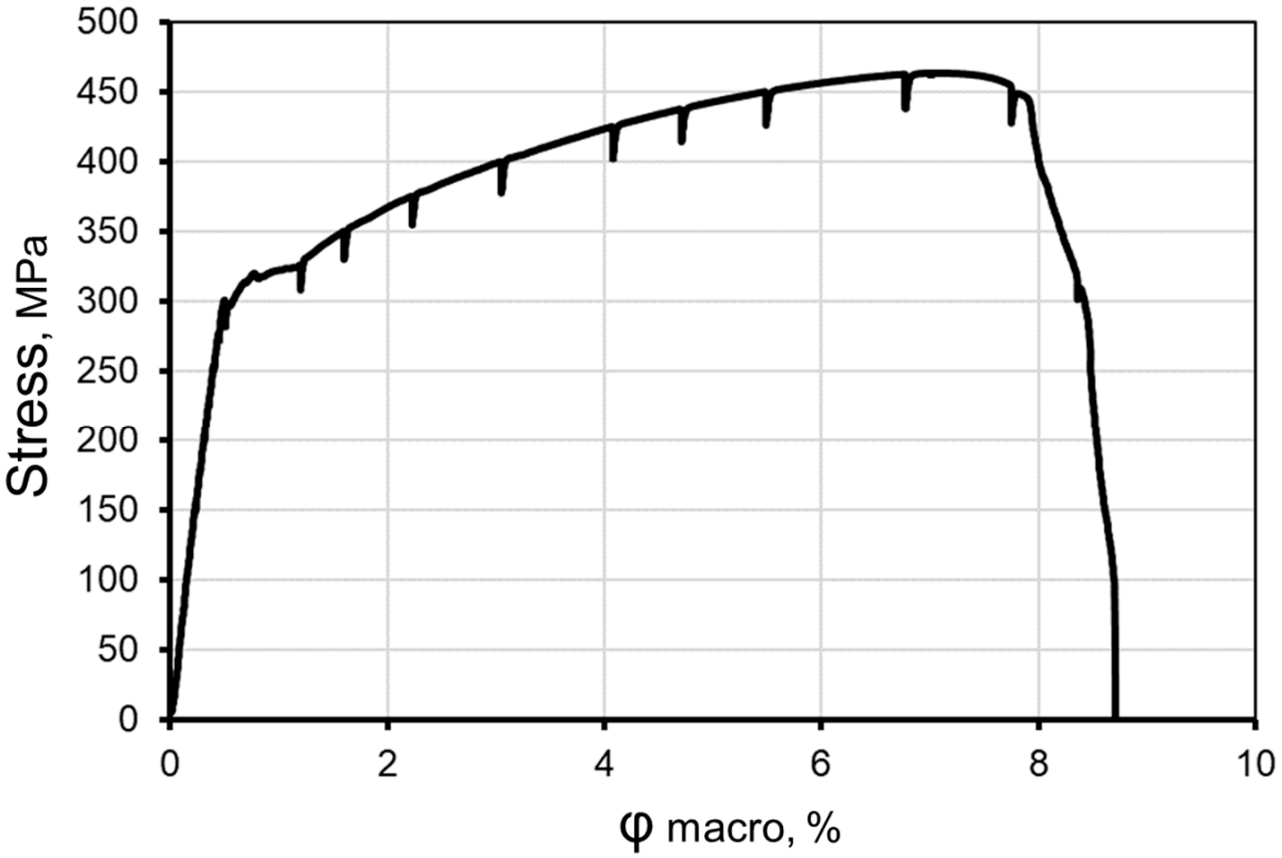

Figure A7. Stress–strain diagram of the tensile specimen.

Based on the data obtained, diagrams were created to compare the meso deformation and micro deformation in different areas of the study with the names of the selected areas (Figure A8). A diagram has also been created to compare macro and micro deformation (Figure A9).

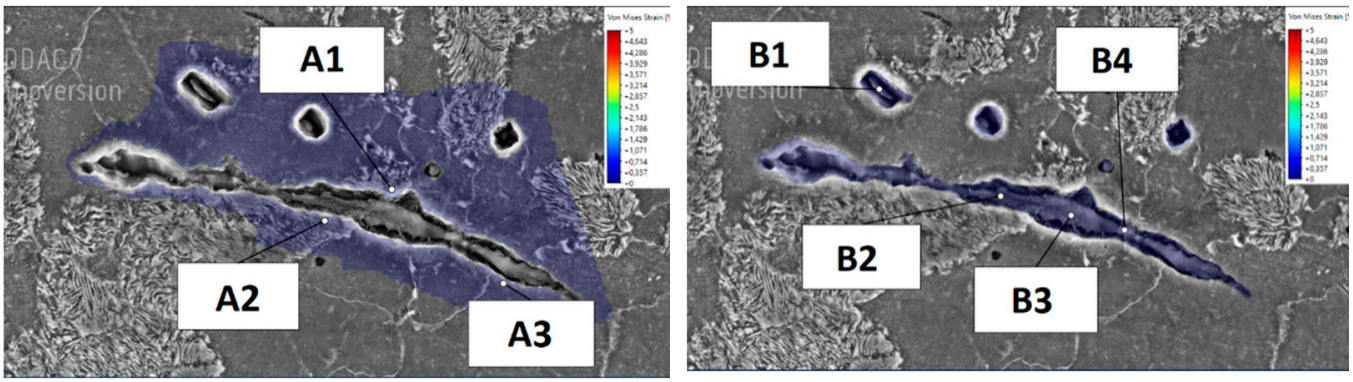

Figure A8. Marking and numbering of measuring points (**a**) around non-metallic inclusions; (**b**) within non-metallic inclusions.

The diagram in Figure A9 shows that the intensity of micro deformation is significantly higher compared to macro deformation at the points far from the pearlite grains.

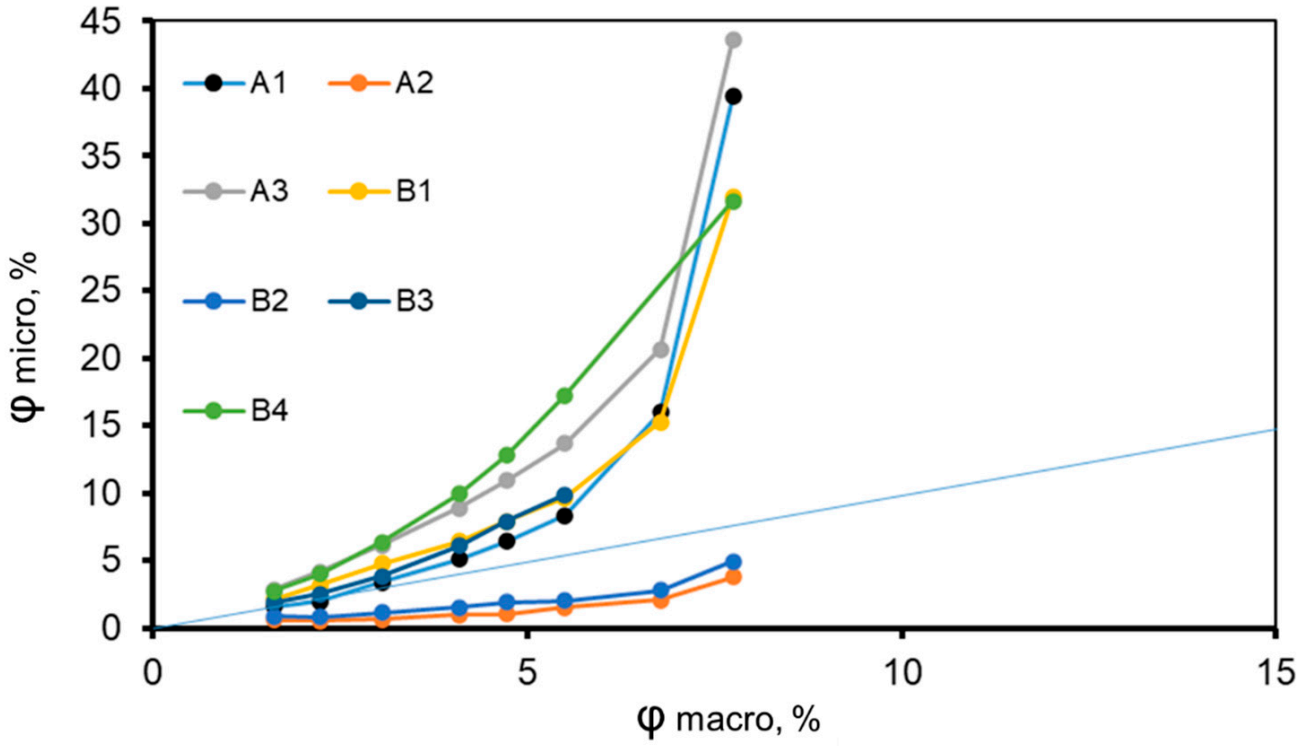

Figure A9. Comparison of meso deformation and micro deformation.

Appendix C. Local Strain Measurement Overlaid on SEM Micrographs

The frame by frame evolution of local strain distribution around (left) and within (right) the MnS inclusion is presented in Figure A10 from 1.6% to 7.75% global true strain.

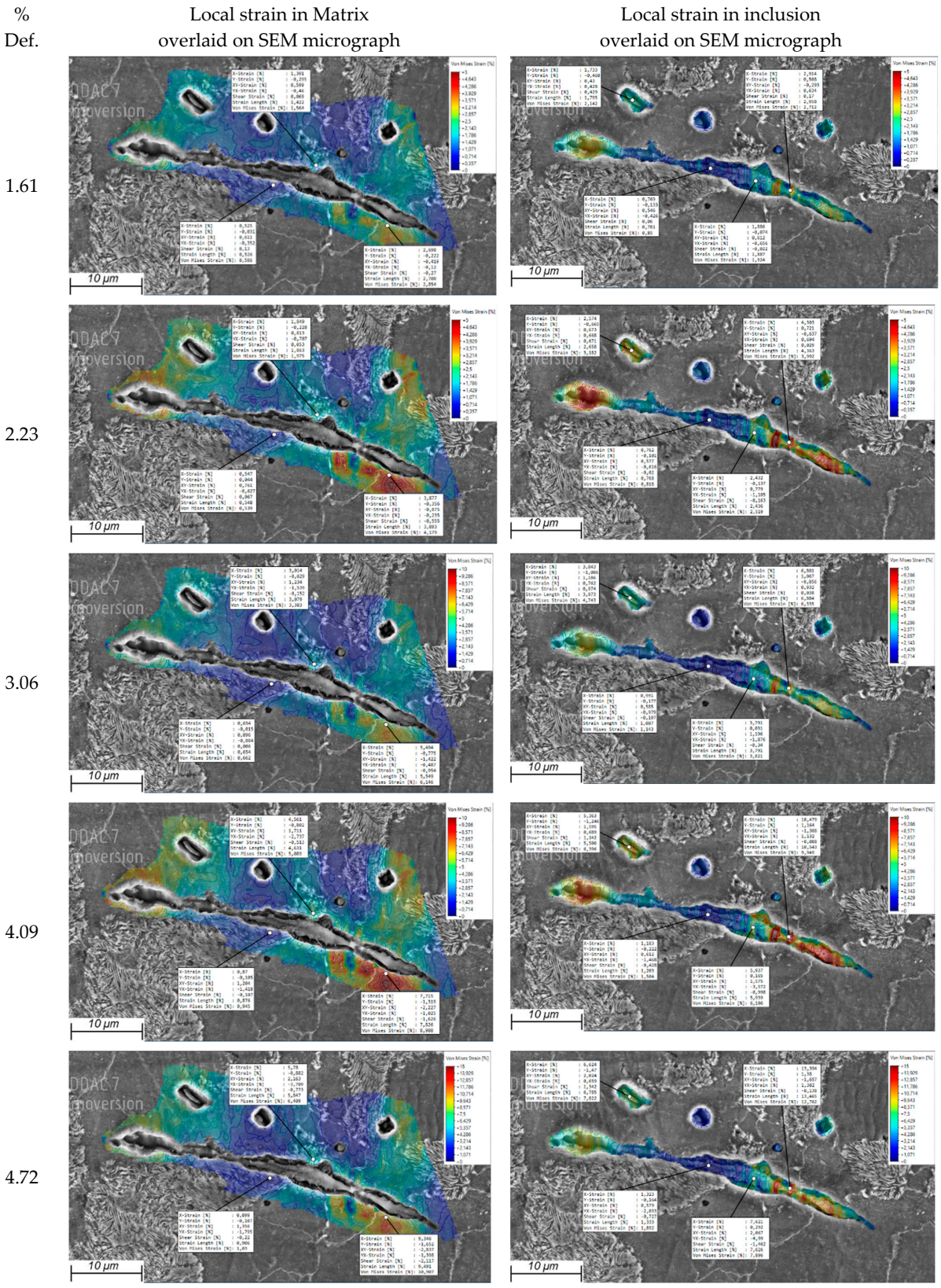

Figure A10. *Cont*.

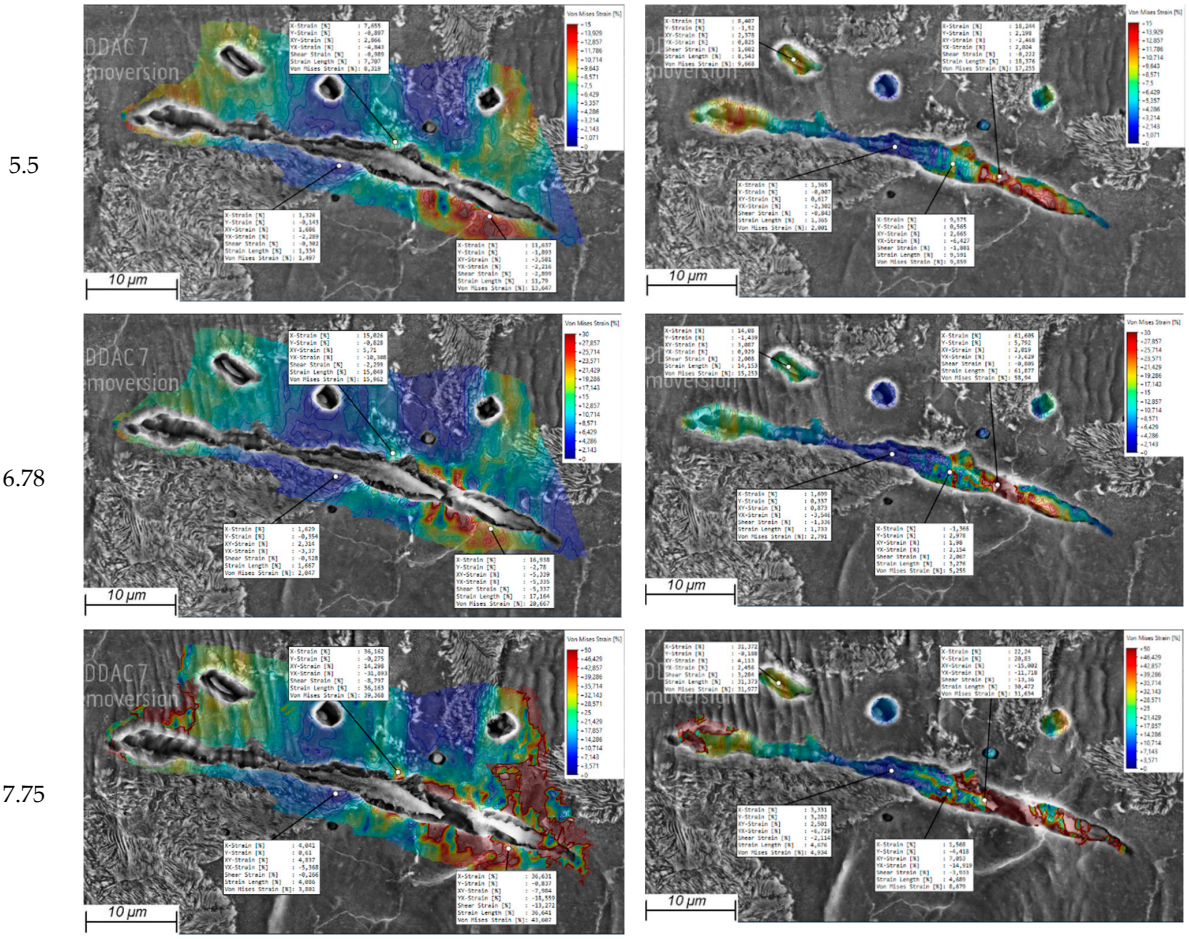

Figure A10. Local strain measurement overlaid on SEM micrographs.

References

1. Krauss, G. *Steels: Processing, Structure, and Performance*; ASM International: Materials Park, OH, USA, 2015.
2. Wang, J.; Shen, Y.; Liu, Y.; Wang, F.; Jia, N. Tailoring Strength and Ductility of a Cr-Containing High Carbon Steel by Cold-Working and Annealing. *Materials* **2019**, *12*, 4136. [CrossRef] [PubMed]
3. Das, T.; Li, J.; Painter, M.; Summerville, E. Evaluation of two AISI 4037 cold heading quality steel wires for improved tool life and product quality. *J. Mater. Eng. Perform.* **2002**, *11*, 86–91. [CrossRef]
4. Shen, P.; Fu, J. Morphology study on inclusion modifications using Mg–Ca treatment in resulfurized special steel. *Materials* **2019**, *12*, 197. [CrossRef] [PubMed]
5. Mohammed, B.; Park, T.; Pourboghrat, F.; Hu, J.; Esmaeilpour, R.; Abu-Farha, F. Multiscale crystal plasticity modeling of multi-phase advanced high strength steel. *Int. J. Solids Struct.* **2018**, *151*, 57–75. [CrossRef]
6. Hosseini, S.; Temmel, C.; Karlsson, B.; Ingesten, N.-G. An in-situ scanning electron microscopy study of the bonding between MnS inclusions and the matrix during tensile deformation of hot-rolled steels. *Metall. Mater. Trans. A* **2007**, *38*, 982–989. [CrossRef]
7. Mukhtar, F.; Qayyum, F.; Shah, M. Studying the effect of thermal fatigue on multiple cracks propagating in an SS316L thin flange on a shaft specimen using a multi-physics numerical simulation model. *Strojniški Vestnik-J. Mech. Eng.* **2019**, *65*, 565–573. [CrossRef]
8. Qayyum, F.; Shah, M.; Muqeet, A.; Afzal, J. The effect of anisotropy on the intermediate and final form in deep drawing of SS304L, with high draw ratios: Experimentation and numerical simulation. *IOP Conf. Ser. Mater. Sci. Eng.* **2016**, *146*, 012031. [CrossRef]
9. Miyamoto, G.; Usuki, H.; Li, Z.-D.; Furuhara, T. Effects of Mn, Si and Cr addition on reverse transformation at 1073 K from spheroidized cementite structure in Fe–0.6 mass% C alloy. *Acta Mater.* **2010**, *58*, 4492–4502. [CrossRef]
10. Khan, U.; Hussain, A.; Shah, M.; Shuaib, M.; Qayyum, F. Investigation of mechanical properties based on grain growth and microstructure evolution of alumina ceramics during two step sintering process. *IOP Conf. Ser. Mater. Sci. Eng.* **2016**, *146*, 012046. [CrossRef]
11. Qayyum, F.; Guk, S.; Kawalla, R.; Prahl, U. Experimental Investigations and Multiscale Modeling to Study the Effect of Sulfur Content on Formability of 16MnCr5 Alloy Steel. *Steel Res. Int.* **2018**, *90*, 1800369. [CrossRef]
12. Chen, H.; Zhou, X. Research progress of gear steel for automobiles. *J. Mater. Sci. Eng.* **2011**, *29*, 478.

13. Sheng, J.; La, P.; Su, J.; Ren, J.; Ma, J.; Shi, Y.; Li, Z.; Wang, J. In situ SEM analysis for deformation mechanism of micro/nanostructured 304 stainless steel with high strength and good plasticity. *Mod. Phys. Lett. B* **2018**, *32*, 1850182. [CrossRef]
14. Salawu, E.Y.; Ajayi, O.O.; Inegbenebor, A.; Popoola, A.; Uyor, U. Effects of Heat Treatment Techniques on the Fatigue Behaviour of Steel Gears: A Review. *J. Phys. Conf. Ser.* **2019**, *1378*, 042001. [CrossRef]
15. Umar, M.; Qayyum, F.; Farooq, M.U.; Khan, L.A.; Guk, S.; Prahl, U. Investigating the Effect of Cementite Particle Size and Distribution on Local Stress and Strain Evolution in Spheroidized Medium Carbon Steels using Crystal Plasticity-Based Numerical Simulations. *Steel Res. Int.* **2020**, *92*, 2000407. [CrossRef]
16. Guk, S.; Hofmann, K.; Beyer, S.; Kawalla, R. Anordnung und Verfahren zur Prüfung des Umformvermögens von Proben aus plastisch umformbaren Werkstoffen und/oder zur Bestimmung der tribologischen Eigenschaften einer vorbehandelten Oberfläche einer Probe. *Patent* **2016**, *10*, 225–530.
17. Kang, Y.-C.; Chan, S.L.-I. Tensile properties of nanometric Al_2O_3 particulate-reinforced aluminum matrix composites. *Mater. Chem. Phys.* **2004**, *85*, 438–443. [CrossRef]
18. Moehring, K.; Walther, F. Load Direction-Dependent Influence of Forming-Induced Initial Damage on the Fatigue Performance of 16MnCrS5 Steel. *Materials* **2020**, *13*, 2680. [CrossRef]
19. Kusche, C.F.; Gibson, J.S.-L.; Wollenweber, M.A.; Korte-Kerzel, S. On the mechanical properties and deformation mechanisms of manganese sulphide inclusions. *Mater. Des.* **2020**, *193*, 108801. [CrossRef]
20. Schowtjak, A.; Wang, S.; Hering, O.; Clausmeyer, T.; Lohmar, J.; Schulte, R.; Ostwald, R.; Hirt, G.; Tekkaya, A.E. Prediction and analysis of damage evolution during caliber rolling and subsequent cold forward extrusion. *Prod. Eng.* **2020**, *14*, 33–41. [CrossRef]
21. Diehl, M.; Groeber, M.; Haase, C.; Molodov, D.A.; Roters, F.; Raabe, D. Identifying Structure–Property Relationships Through DREAM.3D Representative Volume Elements and DAMASK Crystal Plasticity Simulations: An Integrated Computational Materials Engineering Approach. *JOM* **2017**, *69*, 848–855. [CrossRef]
22. Sedighiani, K.; Traka, K.; Roters, F.; Raabe, D.; Sietsma, J.; Diehl, M. Determination and analysis of the constitutive parameters of temperature-dependent dislocation-density-based crystal plasticity models. *Mech. Mater.* **2022**, *164*, 104117. [CrossRef]
23. Hussein, T.; Umar, M.; Qayyum, F.; Guk, S.; Prahl, U. Micromechanical Effect of Martensite Attributes on Forming Limits of Dual-Phase Steels Investigated by Crystal Plasticity-Based Numerical Simulations. *Crystals* **2022**, *12*, 155. [CrossRef]
24. Qayyum, F.; Guk, S.; Kawalla, R.; Prahl, U. On Attempting to Create a Virtual Laboratory for Application-Oriented Microstructural Optimization of Multi-Phase Materials. *Appl. Sci.* **2021**, *11*, 1506. [CrossRef]
25. Zhang, H.; Diehl, M.; Roters, F.; Raabe, D. A virtual laboratory using high resolution crystal plasticity simulations to determine the initial yield surface for sheet metal forming operations. *Int. J. Plast.* **2016**, *80*, 111–138. [CrossRef]
26. Diehl, M.; An, D.; Shanthraj, P.; Zaefferer, S.; Roters, F.; Raabe, D. Crystal plasticity study on stress and strain partitioning in a measured 3D dual phase steel microstructure. *Phys. Mesomech.* **2017**, *20*, 311–323. [CrossRef]
27. Diehl, M.; Wicke, M.; Shanthraj, P.; Roters, F.; Brueckner-Foit, A.; Raabe, D. Coupled Crystal Plasticity–Phase Field Fracture Simulation Study on Damage Evolution Around a Void: Pore Shape Versus Crystallographic Orientation. *JOM* **2017**, *69*, 872–878. [CrossRef]
28. Tasan, C.C.; Hoefnagels, J.P.M.; Diehl, M.; Yan, D.; Roters, F.; Raabe, D. Strain localization and damage in dual phase steels investigated by coupled in-situ deformation experiments and crystal plasticity simulations. *Int. J. Plast.* **2014**, *63*, 198–210. [CrossRef]
29. Wang, D.; Diehl, M.; Roters, F.; Raabe, D. On the role of the collinear dislocation interaction in deformation patterning and laminate formation in single crystal plasticity. *Mech. Mater.* **2018**, *125*, 70–79. [CrossRef]
30. Liu, C.; Shanthraj, P.; Diehl, M.; Roters, F.; Dong, S.; Dong, J.; Ding, W.; Raabe, D. An integrated crystal plasticity–phase field model for spatially resolved twin nucleation, propagation, and growth in hexagonal materials. *Int. J. Plast.* **2018**, *106*, 203–227. [CrossRef]
31. Cereceda, D.; Diehl, M.; Roters, F.; Raabe, D.; Perlado, J.M.; Marian, J. Unraveling the temperature dependence of the yield strength in single-crystal tungsten using atomistically-informed crystal plasticity calculations. *Int. J. Plast.* **2016**, *78*, 242–265. [CrossRef]
32. Shanthraj, P.; Eisenlohr, P.; Diehl, M.; Roters, F. Numerically robust spectral methods for crystal plasticity simulations of heterogeneous materials. *Int. J. Plast.* **2015**, *66*, 31–45. [CrossRef]
33. Roters, F.; Diehl, M.; Shanthraj, P.; Eisenlohr, P.; Reuber, C.; Wong, S.L.; Maiti, T.; Ebrahimi, A.; Hochrainer, T.; Fabritius, H.O.; et al. DAMASK—The Düsseldorf Advanced Material Simulation Kit for modeling multi-physics crystal plasticity, thermal, and damage phenomena from the single crystal up to the component scale. *Comput. Mater. Sci.* **2019**, *158*, 420–478. [CrossRef]
34. Roters, F.; Eisenlohr, P.; Kords, C.; Tjahjanto, D.; Diehl, M.; Raabe, D. DAMASK: The Düsseldorf Advanced MAterial Simulation Kit for studying crystal plasticity using an FE based or a spectral numerical solver. *Procedia IUTAM* **2012**, *3*, 3–10. [CrossRef]
35. Weidner, A.; Yanina, A.; Guk, S.; Kawalla, R.; Biermann, H. Microstructure and Local Strain Fields in a High-Alloyed Austenitic Cast Steel and a Steel-Matrix Composite Material after in situ Tensile and Cyclic Deformation. *Steel Res. Int.* **2011**, *82*, 990–997. [CrossRef]
36. Weidner, A.; Biermann, H. Combination of different in situ characterization techniques and scanning electron microscopy investigations for a comprehensive description of the tensile deformation behavior of a CrMnNi TRIP/TWIP steel. *JOM* **2015**, *67*, 1729–1747. [CrossRef]

37. Weidner, A.; Berek, H.; Segel, C.; Aneziris, C.G.; Biermann, H. In situ tensile deformation of TRIP steel/Mg-PSZ composites. *Mater. Sci. Forum* **2013**, *738–739*, 77–81. [CrossRef]
38. Agnew, S.R.; Brown, D.W.; Tomé, C.N. Validating a polycrystal model for the elastoplastic response of magnesium alloy AZ31 using in situ neutron diffraction. *Acta Mater.* **2006**, *54*, 4841–4852. [CrossRef]
39. Lu, W.; Zhang, D.; Zhang, X.; Wu, R.; Sakata, T.; Mori, H. Microstructural characterization of TiB in in situ synthesized titanium matrix composites prepared by common casting technique. *J. Alloys Compd.* **2001**, *327*, 240–247. [CrossRef]
40. Bachmann, F.; Hielscher, R.; Schaeben, H. Texture analysis with MTEX–free and open source software toolbox. *Solid State Phenom.* **2010**, *160*, 63–68. [CrossRef]
41. Umar, M.; Qayyum, F.; Farooq, M.U.; Guk, S.; Kirschner, M.; Korpala, G.; Prahl, U. Exploring the Structure–Property Relationship in Spheroidized C45EC Steel Using Full Phase Crystal Plasticity Numerical Simulations. *Steel Res. Int.* **2022**, *93*, 2100452. [CrossRef]
42. Pütz, F.; Henrich, M.; Roth, A.; Könemann, M.; Münstermann, S. Reconstruction of Microstructural and Morphological Parameters for RVE Simulations with Machine Learning. *Procedia Manuf.* **2020**, *47*, 629–635. [CrossRef]
43. Huang, Y.; Froyen, L. Quantitative analysis of microstructure in metals with computer assistance. *NDT Net* **2001**, *6*, 5.
44. Lipiński, T.; Wach, A. Dimensional structure of non-metallic inclusions in high-grade medium carbon steel melted in an electric furnace and subjected to desulfurization. *Solid State Phenom.* **2014**, *223*, 46–53. [CrossRef]
45. Ghadbeigi, H.; Pinna, C.; Celotto, S. Quantitative strain analysis of the large deformation at the scale of microstructure: Comparison between digital image correlation and microgrid techniques. *Exp. Mech.* **2012**, *52*, 1483–1492. [CrossRef]
46. Hutchinson, J.W. Bounds and self-consistent estimates for creep of polycrystalline materials. *Proc. R. Soc. Lond. A Math. Phys. Sci.* **1976**, *348*, 101–127.
47. Kalidindi, S.R. Incorporation of deformation twinning in crystal plasticity models. *J. Mech. Phys. Solids* **1998**, *46*, 267–290. [CrossRef]
48. Roters, F.; Eisenlohr, P.; Hantcherli, L.; Tjahjanto, D.D.; Bieler, T.R.; Raabe, D. Overview of constitutive laws, kinematics, homogenization and multiscale methods in crystal plasticity finite-element modeling: Theory, experiments, applications. *Acta Mater.* **2010**, *58*, 1152–1211. [CrossRef]
49. Eisenlohr, P.; Diehl, M.; Lebensohn, R.A.; Roters, F. A spectral method solution to crystal elasto-viscoplasticity at finite strains. *Int. J. Plast.* **2013**, *46*, 37–53. [CrossRef]
50. Qayyum, F.; Guk, S.; Prüger, S.; Schmidtchen, M.; Saenko, I.; Kiefer, B.; Kawalla, R.; Prahl, U. Investigating the local deformation and transformation behavior of sintered X3CrMnNi16-7-6 TRIP steel using a calibrated crystal plasticity-based numerical simulation model. *Int. J. Mater. Res.* **2020**, *111*, 392–404. [CrossRef]
51. Matsuno, F.; Nishikida, S.-i.; Ikesaki, H. Mechanical Properties of Manganese Sulphides in the Temperature Range between Room Temperature and 1000 deg. C. *Trans. Iron Steel Inst. Jpn.* **1985**, *25*, 989–998. [CrossRef]
52. Qayyum, F.; Umar, M.; Guk, S.; Schmidtchen, M.; Kawalla, R.; Prahl, U. Effect of the 3rd Dimension within the Representative Volume Element (RVE) on Damage Initiation and Propagation during Full-Phase Numerical Simulations of Single and Multi-Phase Steels. *Materials* **2021**, *14*, 42. [CrossRef]
53. Gussev, M.; Edmondson, P.; Leonard, K. Beam current effect as a potential challenge in SEM-EBSD in situ tensile testing. *Mater. Charact.* **2018**, *146*, 25–34. [CrossRef]
54. Tasan, C.; Hoefnagels, J.; Geers, M. Microstructural banding effects clarified through micrographic digital image correlation. *Scr. Mater.* **2010**, *62*, 835–838. [CrossRef]
55. Umar, M.; Qayyum, F.; Farooq, M.U.; Khan, L.A.; Guk, S.; Prahl, U. Analyzing the cementite particle size and distribution in heterogeneous microstructure of C45EC steel using crystal plasticity based DAMASK code. In Proceedings of the 2021 International Bhurban Conference on Applied Sciences and Technologies (IBCAST), Islamabad, Pakistan, 12–16 January 2021; pp. 15–20.
56. Needleman, A. A continuum model for void nucleation by inclusion debonding. *J. Appl. Mech.* **1987**, *54*, 525–531. [CrossRef]
57. Diehl, M.; Naunheim, Y.; Yan, D.; Morsdorf, L.; An, D.; Tasan, C.; Zaefferer, S.; Roters, F.; Raabe, D. Coupled Experimental-Numerical Analysis of Strain Partitioning in Metallic Microstructures: The Importance of Considering the 3D Morphology. In Proceedings of the BSSM 12th International Conference on Advances in Experimental Mechanics, Sheffield, UK, 29–31 August 2017; pp. 29–31.
58. Qayyum, F.; Guk, S.; Prahl, U. Studying the Damage Evolution and the Micro-Mechanical Response of X8CrMnNi16-6-6 TRIP Steel Matrix and 10% Zirconia Particle Composite Using a Calibrated Physics and Crystal-Plasticity-Based Numerical Simulation Model. *Crystals* **2021**, *11*, 759. [CrossRef]